Measurement Report: Distinct size dependence and diurnal variation of OA hygroscopicity, volatility, and CCN activity at a rural site in the Pearl River Delta (PRD) region, China

Mingfu Cai[1,2], Shan Huang[1*], Baoling Liang[3], Qibin Sun[3], Li Liu[4*], Bin Yuan[1], Min Shao[1], Weiwei Hu[5], Wei Chen[6], Qicong Song[1], Wei Li[1], Yuwen Peng[1], Zelong Wang[1], Duohong Chen[6], Haobo Tan[4], Hanbin Xu[3], Fei Li[4,7], Xuejiao Deng[4], Tao Deng[4], Jiaren Sun[2], and Jun Zhao[4,8,9]

[1] Institute for Environmental and Climate Research, Jinan University; Guangdong-Hongkong-Macau Joint Laboratory of Collaborative Innovation for Environmental Quality, Guangzhou, 511443, China

[2] Guangdong Province Engineering Laboratory for Air Pollution Control, Guangdong Provincial Key Laboratory of Water and Air Pollution Control, South China Institute of Environmental Sciences, MEE, Guangzhou 510655, China

[3] School of Atmospheric Sciences, Guangdong Province Key Laboratory for Climate Change and Natural Disaster Studies, and Institute of Earth Climate and Environment System, Sun Yat-sen University, Zhuhai, Guangdong 519082, China

[4] Institute of Tropical and Marine Meteorology of China Meteorological Administration, Guangzhou 510640, China

[5] State Key Laboratory of Organic Geochemistry and Guangdong Key Laboratory of Environmental Protection and Resources Utilization, Guangzhou Institute of Geochemistry, Chinese Academy of Sciences, Guangzhou 510640, China

[6] Guangdong Environmental Monitoring Center, Guangzhou 510308, China

[7] Xiamen Key Laboratory of Straits Meteorology, Xiamen Meteorological Bureau, Xiamen 361012, China

26   [8] Southern Marine Science and Engineering Guangdong Laboratory (Zhuhai), Zhuhai, Guangdong

27   519082, China

28   [9] Guangdong Provincial Observation and Research Station for Climate Environment and Air Quality

29   Change in the Pearl River Estuary, Guangzhou, Guangdong 510275, China

30   *Corresponding authors: Shan Huang (shanhuang_eci@jnu.edu.cn) and Li Liu (liul@gd121.cn)

Abstract.

32   Organic aerosol (OA) has a significant contribution to cloud formation and hence climate

33   change. However, high uncertainties still exist in its impact on global climate, owing to the varying

34   physical properties affected by the complex formation and aging processes. In this study, the

35   hygroscopicity, volatility, cloud condensation nuclei (CCN) activity, and chemical composition of

36   particles were measured using a series of online instruments at a rural site in the Pearl River Delta

37   (PRD) region of China in Fall 2019. During the campaign, the average hygroscopicity of OA (κ_{OA})

38   increased from 0.058 at 30 nm to 0.09 at 200 nm, suggesting a higher oxidation state of OA at larger

39   particle sizes, supported by a higher fraction of extremely low volatile OA (ELVOA) for larger size

40   particles. Significantly different diurnal patterns of κ_{OA} were observed between Aitken mode and

41   accumulation mode. For Aitken mode (30-100 nm), the κ_{OA} values showed daily minima (0.02-0.07)

42   during daytime, while exhibited a daytime peak (~0.09) in the accumulation mode. Coincidently, a

43   daytime peak was observed for both aged biomass burning organic aerosol (aBBOA) and less

44   oxygenated organic aerosol (LOOA) based on source apportionment, which were attributed to the

45   aging processes and gas-particle partitioning through photochemical reactions. In addition, the

46   fraction of semi-volatile OA (SVOA) was higher at all measured sizes during daytime than during

47   nighttime. These results indicate that the formation of secondary OA (SOA) through gas-particle

48   partitioning can generally occur at all diameters, while the aging processes of pre-existing particles

49   are more dominated in the accumulation mode. Furthermore, we found that applying a fixed κ_{OA}

50   value (0.1) could lead to an overestimation of the CCN number concentration (N_{CCN}) up to 12%-

51   19% at 0.1%-0.7% supersaturation (SS), which was more obvious at higher SS during daytime.

52   Better prediction of N_{CCN} could be achieved by using size-resolved diurnal κ_{OA}, which indicates that

53   the size-dependence and diurnal variations of κ_{OA} can strongly affect the N_{CCN} at different SS. Our

54   results highlight the need for accurately evaluating the atmospheric evolution of OA at different size

55   ranges, and their impact on the physicochemical properties and hence climate effects.

57   1.   Introduction

58   The impact of aerosol particles on global climate is widely known, including absorbing and

59   scattering solar radiation, and acting as cloud condensation nuclei (CCN). However, the extent of

60   their contribution on the climate forcing is still unclear. Organic aerosol (OA) as a dominant

61   component of fine particles (Jimenez et al., 2009), may contribute the uncertainties of climate effects

62   of particles, mainly owing to unknown sources, physical properties, formation, and aging

63   mechanisms (Volkamer et al., 2006;Kuang et al., 2020b;Rastak et al., 2017). Numerous studies show

64   that secondary organic aerosol (SOA) accounts for a large OA fraction in most atmospheric

65   environments (e.g., Huang et al., 2014;Shrivastava et al., 2017;Kanakidou et al., 2005;Hallquist et

66   al., 2009). Nevertheless, both primary OA (POA) and SOA in the ambient air remain poorly

67   characterized in terms of the formation mechanism and atmospheric evolution, and their particle

68   diameter can vary on a large scale. Their impact on the global climate and atmospheric chemistry is

69   still highly uncertain.

70   A combination of Aerodyne Aerosol Mass Spectrometer (AMS) or Aerosol Chemical Species

71   Monitor (ACSM) with positive matrix factorization (PMF) is widely used for investigating the OA

72   evolution in the atmosphere (Li et al., 2013;Huang et al., 2018;Huang et al., 2014;Chen et al.,

73   2015;Jimenez et al., 2009). For instance, Qin et al. (2017) found that hydrocarbon-like OA (HOA)

74   from traffic emission contributed up to 40% of OA during nighttime, owing to daytime traffic

75   restrictions on heavy vehicles in urban Guangzhou. Kuang et al. (2020a) reported a dominant

76   contribution to oxygenated OA (OOA) through aqueous-phase reaction in the North China Plain

77   (NCP). Guo et al. (2020) observed different SOA mechanisms between clean and pollution episodes

78   in the Pearl River Delta (PRD) region. Nevertheless, the investigation of bulk OA is still insufficient

79   in understanding the aerosol climate effects without the size-resolved characterization. The OA size

80   distribution is largely dependent on its composition, sources and aging level. Li et al. (2012)

81   observed various mass distribution patterns for different species in airborne particulate organics and

82   reported that dehydrated sugars, fossil fuel-derived *n*-alkanes, and PAHs showed a unimodal

83   distribution, while non-dehydrated sugars and plant wax was derived as n-alkanes which presented

84   a bimodal pattern. In the urban region, Aitken mode was mainly dominated by HOA owing to traffic

85   emissions (Zhang et al., 2005b;Cai et al., 2020). In the marine atmosphere, the size distribution of

86   fine mode POA was found to be independent of sea salt, while coarse mode particles tended to be

87   internally mixed with sea salt (Gantt and Meskhidze, 2013). Similarly, the OA physical properties

88   were also found to be size-dependent. Deng et al. (2018) reported a higher OA hygroscopicity

89   ($\kappa_{OA} \approx 0.22$) at about 150 nm than that ($\kappa_{OA} \approx 0.19$) at sub-100 nm at a forest site. In contrast, Zhao

90   et al. (2015) measured size-dependent hygroscopicity and chemical composition for SOA from

91   various procedures and found that κ_{OA} of SOA from α-pinene photooxidation decreased from 0.17

92   at 50 nm to 0.07 at 200 nm, which was attributed to the higher oxidation degree for smaller particles.

93   The size dependence of OA properties in the aforementioned studies might exert impact on the

94   CCN prediction, which is mainly determined by their sources and formation processes. Cai et al.

95   (2018) found that N_{CCN} at 0.1% SS was underestimated by about 10% if a κ_{OA} value of 0.1 was used.

96   A model simulation from Liu and Wang (2010) showed that an increase of about 40-80% for the

97   CCN concentration was obtained by increasing the κ value of POA from 0 to 0.1. Wang et al. (2008)

98   reported that the uncertainties of the first indirect aerosol effect varied from -0.2 to 0.2 W m^{-2} for a

99   κ_{OA} value of 0 to 0.25. Rastak et al. (2017) showed that using a single-parameter framework of κ_{OA}

100   in evaluating the climate effects of aerosol could lead to significant errors (about -1.02 W m^{-2}),

101   which is the same order as the climate forcing of anthropogenic aerosol during the industrial period.

102   These results further highlight a need for the understanding of the relationship between the OA

103   evolution processes and its impact on the CCN activity at different particle sizes.

104   The OA hygroscopicity and volatility can provide information about the evolution of OA, given

105   that they are often related to the chemical composition of the particles. A positive correlation

106   between the hygroscopicity values and the oxidation degree of OA, including the ratio of atomic

107   oxygen to atomic carbon (O:C), the oxidation state ($\overline{OS_C}$), or the mass fraction of m/z 44 (for CO_2^+)

108   ion fragments in the organic spectra (f_{44}) from chemical composition, were widely reported in the

109   literature (Wu et al., 2013;Pajunoja et al., 2015;Chang et al., 2010). Kim et al. (2020) found that the

110   κ_{OA} was positively and negatively correlated with OOA and HOA at different size ranges,

111   respectively. Deng et al. (2019) reported a decreasing trend of κ_{OA} at a size range of 100-360 nm

112   during daytime in a forest environment, suggesting the formation of biogenic SOA (BSOA) through

113   photochemical oxidation of biogenic volatile organic compounds (BVOCs). The OA volatility,

114   specifically saturation vapor concentration (C^*), is linked to the gas-particle partitioning and aging

115   processes. In general, the C^* value decreases with an increase of the oxidation degree and the

116   number of atomic carbon (Donahue et al., 2011). May et al. (2013) found that most of the biomass-

117 burning POA were semi-volatile. Saha et al. (2017) showed a lower volatility of OA in the afternoon

118 hours using a dual-thermodenuder (TD) system, probably owing to photochemical oxidation of OA.

119 Hong et al. (2017) derived the OA volatility distribution by a combination of the VTMDA

120 measurement and a multi-component evaporation dynamics model, and found a moderate ($R \approx 0.4$)

121 correlation between the OA groups obtained by the VTDMA data and the PMF results, respectively.

122 In this study, we investigate physical properties of OA at different size ranges, and evaluate

123 their influence on the atmospheric CCN concentration. A rural field measurement was conducted at

124 the Heshan site in the Pearl River Delta (PRD) region, China, during Fall 2019 (October and

125 November). The hygroscopicity, volatility, size-resolved CCN activity, and chemical composition

126 were measured by a series of online instruments. The size-resolved hygroscopicity and volatility

127 distribution of organics was investigated. PMF was employed to analyze the sources and processes

128 of OA. The impact of diurnal variation and size dependence of κ_{OA} on the N_{CCN} prediction at

129 different supersaturation (SS) was assessed.

130 **2. Measurement and methodology**

131 **2.1 Measurement site**

132 The field measurements were conducted at the Heshan supersite in the Guangdong province,

133 China during autumntime 2019 (27th September to 17th November 2019). This supersite (22°42′39.

134 1″N, 112°55′35.9″E) is located at the southwest of the PRD region and surrounded by farms and

135 villages, with an altitude of about 40 m. All sample particles first passed through a Nafion dryer

136 (Model MD-700, Perma Pure Inc., USA) to maintain a relative humidity (RH) lower than 30%. The

schematic diagram of the experimental setup can be found in Fig. S1. Detailed descriptions of the

measurement site and some instruments can be found in Cai et al. (2021a).

2.2 Instrumentation

2.2.1   Aerosol hygroscopicity and volatility measurement

Size-resolved hygroscopicity and volatility of particles were measured by a H/V-TDMA

(model M3000, Bmet Inc., China). The instrument consists of two differential mobility analyzers

(DMA1 and DMA2, model 3081 L, TSI Inc., USA), a Nafion humidifier (Model MD-700, Perma

Pure Inc., USA), a heater tube, and a condensation particle counter (CPC, model 3788, TSI Inc.,

USA). The instrument was operated in H- and V- mode during the measurement with a cycle time

of about 3-4 h. The dried sample particles were firstly charged by an X-ray neutralizer and then

classified by DMA1 at six diameters (30, 50, 80, 100, 150, and 200 nm). In the H-mode, the chosen

particles with a specific dry diameter (D_0) were sequentially humidified by the Nafion humidifier

to achieve 90% of RH. A combination of DMA2 and CPC were employed to measure the size

distribution of humidified particles (Dp_{wet}). The hygroscopic growth factor (GF) at a certain dry

diameter can be defined as:

$$GF(D_0) = \frac{Dp_{wet}}{D_0} \tag{1}$$

In the V-mode, the selected particles from DMA1 were heated in the heater tube at 100, 150,

200, and 250°C, respectively. Similar to the H mode, the size distribution of heated particles along

with particles at room temperature (25°C) was measured by the DMA2 and CPC. The volatility

shrink factor (VSF) at a certain diameter and temperature is then defined as:

157 $$VSF(T, D_0) = \frac{Dp(T)}{D_0} \qquad (2)$$

158   Before the campaign, standard polystyrene latex spheres (PSLs; with a size of 20, 50, and 200

159 nm), ammonium sulfate, and sodium chloride were used to calibrate the diameter classification of

160 DMAs, hygroscopicity measurement, and the transport efficiency of particles in the heater tube,

161 respectively. For the H/V-TDMA data, the TDMAfit algorithm (Stolzenburg and McMurry, 2008)

162 was applied to fit the growth factor and volatility shrink factor probability density function (GF-

163 PDF and VSF-PDF) with various DMA transfer functions. The detailed data inversion processes

164 can be found in Tan et al. (2013a).

165 **2.2.2   The size-resolved CCN activity and particle number size distribution measurement**

166   A combination of a cloud condensation nuclei counter (CCNc, model 200, DMT Inc., USA)

167 and a scanning mobility particle sizer (SMPS, model 3938L75, TSI Inc., USA) was employed to

168 measure size resolved CCN activity. The supersaturation (SS) of each column (A and B) of CCNc

169 was set to be 0.1%, 0.2% and 0.4% (for column A), and 0.7%, 0.9% and 1.0% (for column B),

170 respectively. During the measurement, the SMPS was operated at a scanning mode. The sample

171 particles were firstly neutralized by an X-ray neutralizer (model 3088, TSI Inc., USA) and were

172 subsequently classified by a DMA. The classified particles were then split into three paths: one to a

173 CPC (model 3756, TSI Inc., USA) for measurement of particle number concentration (with a flow

174 rate of 0.6 LPM) and two to the CCNc for measurement of the CCN number concentration (N_{CCN})

175 at a specific SS (with a flow rate of 0.5 LPM).

176   The particle number size distribution (PNSD) in a size range of 1 nm-10 μm was measured by

177 a suite of instruments including a diethylene glycol scanning mobility particle sizer (DEG-SMPS,

178   model 3938E77, TSI Inc., USA), a SMPS (model 3938L75, TSI Inc., USA), and an aerodynamic

179   particle sizer (APS, model 3321, TSI Inc., USA). The detailed description of these instruments can

180   be found in Cai et al. (2021a). Before the measurement, the SMPSs were calibrated with PSLs (20,

181   50 and 200 nm) and the CCNc was calibrated with ammonium sulfate ($(NH_4)_2SO_4$) particles at

182   selected SSs (0.1%, 0.2%, 0.4%, 0.7%, 0.9%, and 1.0%, Sect. S1).

183   **2.2.3   Aerosol chemical composition measurement**

184   The size-resolved chemical composition of ambient aerosol particles was measured by a soot

185   particle aerosol mass spectrometer (SP-AMS, Aerodyne Research, Inc., USA). The principle and

186   operation of the instrument are generally the same as a high resolution time-of-flight aerosol mass

187   spectrometer (HR-ToF-AMS) (Canagaratna et al., 2007). In addition to an original tungsten

188   vaporizer (~600°C), a soot-particle module which mainly contains a Nd:YAG (1064 nm) laser was

189   integrated into HR-ToF-AMS for vaporizing refractory species (Onasch et al., 2012). As a result,

190   SP-AMS can provide chemical information for non-refractory species (nitrate, sulfate, ammonium,

191   chloride, and organics) as well as refractory species such as refractory black carbon (rBC) and

192   several metals. During the campaign, SP-AMS was run between V mode (only tungsten vaporizer)

193   and SP mode (tungsten and laser vaporizers) with a time resolution of 1 min. In order to minimize

194   disturbance caused by mode switch, 15 min averaged data are used in the present study. More details

195   on the quantification using ionization efficiency, composition dependent collection efficiency and

196   external instrument as well as software for SP-AMS data analysis could be found in Kuang et al.

197   (2021).

198   Facilitated by the time-of-flight chamber in SP-AMS, the particle mass size distribution can be

199   measured in submicrometer size range, specifically, 40 to 800 nm in vacuum aerodynamic diameter

200   (Dva). The mass size distribution for relevant AMS species was used in this study for investigating

201   the link between particle chemical composition and volatility/hygroscopicity. Since SP-AMS

202   provided the size distribution versus Dva, the equation below was used to convert Dva into mobility

203   diameter (Dp).

204      $$D_p = \frac{D_{va}}{S \times \frac{\rho_p}{\rho_0}} \tag{3}$$

205   where S is the shape factor, ρ_p is the particle density, and ρ_0 is the density for water (1 kg m^{-3}). In

206   this study, we estimate that the particles were close to sphere due to high RH in the PRD and thus a

207   shape factor of 0.8 was applied. An overall particle density of 1.6 kg m^{-3} is used.

208   Based on high resolution data from SP-AMS, source apportionment was performed for organic

209   aerosols (OA) in the bulk PM$_1$ with positive matrix factorization (PMF, Paatero, 1997;Paatero and

210   Tapper, 1994) following the instruction in Ulbrich et al., 2009. The input data, selection of solutions,

211   mass spectral profile, and time series of each factor can be found in Kuang et al. (2021). In brief,

212   OA measured at the Heshan site could be divided into six components with identified sources and

213   processes, including two from primary sources and four factors corresponding to secondary

214   formation: a hydrocarbon-like OA (HOA) contributed mainly by vehicle exhausts mixed with

215   cooking emissions, a biomass burning OA (BBOA) related to biomass burning combustion from the

216   surrounding villages, an aged BBOA (aBBOA), a more oxygenated OA (MOOA) from regional

217   transport, a less oxygenated OA (LOOA) provided by daytime photochemical formation, and a

218   nighttime-formed OA (Night-OA) related to secondary formation during nighttime.

2.3 Methodology

2.3.1 Estimates of hygroscopicity

The hygroscopicity parameter κ can be obtained under subsaturation condition by the H/V-TDMA measurement and supersaturation condition by the CCNc measurement. The κ value (κ_{HTDMA}) can be estimated from the growth factor measured by H/V-TDMA (Petters and Kreidenweis, 2007):

$$\kappa_{HTDMA} = (GF^3 - 1)\left[\frac{1}{RH}\exp\left(\frac{4\sigma_{s/a}M_w}{RT\rho_w D_p} - 1\right)\right] \tag{4}$$

where $\sigma_{s/a}$ is the surface tension of the solution/air interface and the solution is temporarily assumed to be pure water (0.0728 N m^{-1} at 298.15 K), M_w is the molecular weight of water (0.018 kg mol^{-1}), R is the universal gas constant (8.314 J mol^{-1} K^{-1}), T is the thermodynamic temperature in Kelvin (298.15 K), ρ_w is the density of water (about 997.04 kg m^{-3} at 298.15 K) and D_p is the particle diameter in meters.

For the CCNc measurement, the κ value (κ_{CCN}) is calculated from the critical supersaturation (Sc) and the critical diameter (D_{50}) by the following equation (Petters and Kreidenweis, 2007):

$$\kappa_{CCN} = \frac{4A^3}{27D_{50}^3(\ln Sc)^2}, A = \frac{4\sigma_{s/a}M_w}{RT\rho_w} \tag{5}$$

The critical diameter, D_{50}, is defined as the diameter at which 50% of the particles are activated at a specific SS, and can be obtained from the N_{CCN} and N_{CN} measured by the CCNc and SMPS system:

$$\frac{N_{CCN}}{N_{CN}} = \frac{B}{1+(\frac{D_p}{D_{50}})^c} \tag{6}$$

where the B and C are fitting coefficients.

239 **2.3.2   Derivation of the size-resolved hygroscopicity of organic matter**

240   The size-resolved chemical composition is adopted to derive the size-dependent hygroscopicity

241 of organic matter (κ_{OA}). However, the AMS cannot provide sufficient information of the size-

242 resolved species, especially for small size particles (< 100 nm) owing to the low mass concentration.

243 Thalman et al. (2017) proposed a method to reconstruct the size-resolved chemical composition,

244 which combines a time-resolved bulk mass concentration and an average mass distribution.

245 Nevertheless, the variation of mass distribution was not considered in this method. In this study, a

246 bimodal lognormal distribution function method was adopted and the one-hour average mass

247 distribution was fitted to obtain the reconstructed size-resolved chemical composition. The average

248 mass distribution with bimodal lognormal fitted modes of each species was shown in Fig. S2.

249   According to the ZSR mixing rule (Zdanovskii, 1948;Stokes and Robinson, 1966), the

250 hygroscopicity of particles (κ_{AMS}) can be calculated based on the SP-AMS measurement, assuming

251 an internal mixing state for all particles:

252      $\kappa_{AMS} = \sum_i \kappa_i \varepsilon_i$ (7)

253 where κ_i is the κ value of each component and ε_i is the volume fraction of corresponding species in

254 particles. The mole concentrations of the inorganic species are estimated based on the NH_4^+, SO_4^{2-},

255 and NO_3^- measured by the AMS (Gysel et al., 2007):

256      $n_{NH_4NO_3} = n_{NO_3^-}$

257      $n_{H_2SO_4} = max\,(0, N_{SO_4^{2-}} - n_{NH_4^+} + n_{NO_3^-})$

258      $n_{NH_4HSO_4} = min\left(2n_{SO_4^{2-}} - n_{NH_4^+} + n_{NO_3^-}, n_{NH_4^+} - n_{NO_3^-}\right)$

259      $n_{(NH_4)_2SO_4} = max\left(n_{NH_4^+} - n_{NO_3^-} - n_{SO_4^{2-}}, 0\right)$

260 $$n_{HNO_3} = 0 \qquad\qquad\qquad (8)$$

261 where n denotes the number of moles of each component (NH$_4^+$, SO$_4^{2-}$ and NO$_3^-$), ε_{org} and ε_{BC}

262 were obtained from mass concentration measured by the SP-AMS. The density and κ value of each

263 component were listed in Table 1.

264 The κ$_{OA}$ can be calculated based on the size-resolved chemical composition and H/V-TMDA

265 measurement using following equation:

266 $$\kappa_{OA} = \frac{\kappa_{HTDMA} - (\kappa_{inorgsalt}\varepsilon_{inorgsalt} + \kappa_{BC}\varepsilon_{BC})}{\varepsilon_{org}} \qquad\qquad (9)$$

267 **2.3.3   Volatility data**

268 During the heating process, some particles could be lost between DMA$_1$ and DMA$_2$ due to

269 complete evaporation (CV), thermophoresis, and Brownnian diffusion (Philippin et al., 2004).

270 Owing to these losses, the V-mode measurement does not represent the actual volatility distribution

271 of the monodisperse particles. The sodium chloride (NaCl) particles, which do not evaporate at the

272 set temperature in this measurement, were used to determine the particle losses owing to

273 thermophoretic forces and diffusion. The size- and temperature-dependent transmission efficiency

274 ($\eta(D_p, T)$) of NaCl in the heater was shown in Fig. S3. Thus, the number fraction of CV group

275 ($NF_{CV}(D_p, T)$) at a certain diameter and temperature can be calculated using the following equation

276 (Cheung et al., 2016):

277 $$NF_{CV}(D_p, T) = 1 - \frac{N'(D_p, T)}{N(D_p)\eta(D_p, T)} \qquad\qquad (10)$$

278 where $N'(D_p, T)$ is the number concentration of particles at a specific diameter and temperature

279 after heating, which was measured by the CPC in the H/V-TDMA. The $N(D_p)$ is the number

280 concentration of particles with a diameter D_p before heating, which was provided by the SMPS

281 measurement. The volume fraction remaining (VFR) after heating for the measured particles can be

282 obtained according to the following equation:

283
$$VFR(D_p, T) = \sum_i VSF_i^3(D_p, T) \, NF_i(D_p, T) \left[1 - NF_{CV}(D_p, T)\right] \tag{11}$$

284 where i represents the ith VSF bin, and NF_i is the number fraction of particles with VSF_i, which is

285 calculated based on the VSF-PDF ($c(VSF, D_p, T)$):

286
$$NF_i = \int_{VSF_i}^{VSF_{i+1}} c(VSF, D_p, T) \, dVSF \tag{12}$$

287 The mass fraction remaining (MFR) was assumed to be proportional to VFR, assuming that

288 the density of particles was constant before and after heating.

289 **2.3.4 Multi-component evaporation dynamics model**

290 Based on the volatility basis set (VBS) framework (Donahue et al., 2011), the organic matter

291 was classified into three organic groups based on the saturation concentration (C*(T_{ref}),

292 T_{ref}=298.15 K): extremely low volatility organic aerosol (ELVOA, $C^*=10^{-5}$ μg m^{-3}), low volatility

293 organic aerosol (LVOA, $C^*=10^{-2}$ μg m^{-3}), and semi-volatility organic aerosol (SVOA, $C^*=10$ μg m^{-}

294 ^{3}).

295 A multi-component evaporation dynamics model described by Lee et al. (2011) was used to

296 simulate the evaporation of particles in the heated tube of the H/V-TDMA by solving the mass

297 transfer regime equation, in order to obtain the size-resolved distribution of the aforementioned

298 three OA groups. The MFR, residence time (about 4.11 s) in the heater tube, the temperature of the

299 heater tube, particle number concentration, particle sizes, chemical composition, and

300 thermophysical properties of each species (Table 2) were input into the model. The particles were

301 assumed to be internally mixed with organic and inorganic species, including three organic groups,

302 NH$_4$NO$_3$, (NH$_4$)$_2$SO$_4$, and black carbon (BC). The mass transfer of each component i between the

303 aerosol and gas phases in the transition regime was calculated from the following equation:

304 $$\frac{dm_{p,i}}{dt} = 2\pi D_i D_p f(Kn, \alpha)(C_{i,g} - f_i C_i^*(T) exp\left(\frac{4\sigma_{s/a} M_i}{D_p \rho_i RT}\right))$$

305 $$\frac{dC_{i,g}}{dt} = -\frac{dm_{p,i}}{dt} N_p(D_p) \tag{13}$$

306 where $m_{p,i}$ (µg) is the mass of species i in a single particle, $C_{i,g}$ (µg m^{-3}) is its gas-phase

307 concentration, D_i (m^2 s^{-1}) is the diffusion coefficient for species i in air, D_p (m) is the particle

308 diameter, $f(Kn, \alpha)$ is a correction term to account for non-continuum mass transfer depending on

309 Knudsen number (Kn) and mass accommodation coefficient (α), f_i is the mole fraction of species

310 i, $C_i^*(T)$ is the saturation concentration at temperature (T) of the heater tube, M_i (kg mol^{-1}) is the

311 molecular weight of species i, ρ_i (kg m^{-3}) is its density and $N_p(D_p)$ (cm^{-3}) is the number

312 concentration of particles with a diameter D_p.

313 The correction term $f(Kn, \alpha)$ is determined by the following equation (Seinfeld and Pandis,

314 2016):

315 $$f(Kn, \alpha) = \frac{1 + Kn}{1 + 2Kn(1 + Kn)/\alpha}$$

316 $$Kn = \frac{2\lambda_i}{D_p} \tag{14}$$

317 where λ_i is the mean free path of species i in the air, which is defined as $\lambda_i = \frac{2D_i}{c_i}$. The c_i is the mean

318 speed of species i and $c_i = \sqrt{\frac{8RT}{\pi M_i}}$.

319 The temperature-dependent $C_i^*(T)$ is estimated from the Clausius-Clapeyron equation:

320 $$C_i^*(T) = C_i^*(T_{ref}) exp\left[\frac{\Delta H_{vap,i}}{R}\left(\frac{1}{T_{ref}} - \frac{1}{T}\right)\right]\frac{T_{ref}}{T} \tag{15}$$

321 where $\Delta H_{vap,i}$ (kJ mol^{-1}) is the enthalpy of vaporization. The known mass fractions of NH$_4$NO$_3$,

322 (NH$_4$)$_2$SO$_4$, and BC were calculated respectively, based on the SP-AMS measurement. The time

323 step of the model was set to be 10^{-3} s. The characteristics of each species were listed in Table 2. The

324   mass fraction of each organic group in different particle sizes was derived by minimizing the squared

325   residuals (SSR) values, $SSR = \sum_{T_i=T_1}^{T_5}[MFR_{model}(T_i, Dp) - MFR_{measured}(T_i, Dp)]^2$. The non-

326   linear constrained optimization function "fmincon" in MATLAB (version 2016a, Mathworks Inc.)

327   was used to obtain the optimal fitted result. A constrained of $\sum f_{i,inorganics} + \sum f_{i,organics} = 1$ is used.

328   The modeled MFR is strongly dependent on the values of vaporization enthalpy (ΔH_{vap}) and

329   mass accommodation coefficient (α) (Lee et al., 2010;Lee et al., 2011). Thus, a sensitivity test is

330   performed to determine the ΔH_{vap} of OA and α based on the campaign average data (Fig. S4). A

331   linear relationship was adopted between ΔH_{vap} and $log_{10} C_i^*(T_{ref})$, $\Delta H_{vap} = -a \cdot$

332    $log_{10} C_i^*(T_{ref}) + b$, where a and b are fitting parameters (Epstein et al., 2010). The a and b values

333   are set to be [0, 4, 8, 12] and [50, 80, 100, 150, 200] in the sensitivity test, respectively, along with

334   α = [0.01, 0.09, 0.1, 0.5, 0.7, 0.9, 1]. The results show that the measured MFR was reproduced well

335   (with the lowest SSR of 0.0205, Fig. S5) by using ΔH_{vap}=80 kJ mol^{-1} with α of 0.09, 0.1 and 0.7,

336   respectively. For simplicity, ΔH_{vap}=80 kJ mol^{-1} and α=0.09 are considered as the best estimation

337   and adopted in the simulation of the whole campaign datasets. The extracted α value was consistent

338   with the values ($\alpha \leq 0.1$) reported previously (Saha et al., 2015;Park et al., 2013;Saleh et al.,

339   2008;Cappa and Jimenez, 2010), indicating significant resistance to mass transfer during

340   evaporation. In addition, the ΔH_{vap} of OA is of the same magnitude (80-150 kJ mol^{-1}) as reported

341   in the literature (Hong et al., 2017;Saha et al., 2017;Riipinen et al., 2010).

342   Note that the decomposition of particles during the heating process is ignored in the model.

343   Kiyoura and Urano (1970) suggested that ammonium sulfate would decompose to ammonium

344   bisulfate (NH_4HSO_4) or triammonium hydrogen sulfate ($(NH_4)_3H(SO_4)_2$), and ammonia (NH_3) when

345   heated to around 160-180 °C. Wang and Hildebrandt Ruiz (2018) also observed thermal

346 decomposition of organics and ammonium sulfate during evaporation by using a Filter Inlet for

347 Gases and AEROsols chemical-ionization mass spectrometer (FIGAERO-CIMS). It suggests that,

348 besides sublimation, decomposition might occur during evaporation of particles. However, the

349 mechanisms of decomposition are complex and remain unclear, which is difficult to simulate in our

350 model. We roughly estimated uncertainty caused by the decomposition and found that ignoring the

351 decomposition of organics would lead to an underestimation of SVOA, while the decomposition of

352 $(NH_4)_2SO_4$ played a minor role in the simulation (Sect. S2). However, the exact effects are still

353 highly uncertain. We hence exclude the decomposition of particles from the model for simplicity.

354 **3   Results and discussion**

355 **3.1 Overview**

356   Figure 1 shows the temporal profile of PNSD (a), aerosol chemical composition and total mass

357 concentration of PM$_{2.5}$ (b), mass fraction of each component (c), and wind speed and direction (d)

358 during the measurements. Note that the SP-AMS measurement started on 12th October. According

359 to the PNSD data, a total number of 20 new particle formation (NPF) events were observed during

360 the whole campaign. The background particles mainly exhibited unimodal distribution which

361 peaked at a size range of about 80-150 nm. The average particle number concentration (N_{CN}) in the

362 size range of 3-1000 nm was about 12700 cm^{-3}, much lower than that from the rural measurement

363 (18150 cm^{-3}) in 2006 in the PRD region (Rose et al., 2010). A wide accumulation mode was

364 observed during the period prevalent with north wind direction, implying that the air mass from the

365 north could bring pollutants from the city cluster around Guangzhou to the measurement site.

366   The chemical composition and the corresponding mass fraction measured by the SP-AMS (Fig.

367   1 b and c) were consistent with those of PNSD, which showed a significantly high mass

368   concentration of organics when the wind was from the north. The average mass fraction of PM_1 was

369   dominated by organics (51.8%), followed by sulfate (17.5%), nitrate (10.2%), BC (9.9%),

370   ammonium (8.8%), and chloride (1.7%). The mass concentration of organics varied from 3.3 to

371   123.4 μg m^{-3}, with an average value of 20.3 μg m^{-3}, lower than the value (25.7 μg m^{-3}) reported in

372   Guangzhou city (Qin et al., 2017), but significantly higher than that was observed (4.1 μg m^{-3}) in

373   Hong Kong (Lee et al., 2013). The mass distribution of the chemical species at the Heshan site was

374   similar to that measured in inland China (Chen et al., 2015;Huang et al., 2014), which was

375   dominated by organics from anthropogenic emissions. A distinguished and reproducible diurnal

376   pattern of the mass fraction was observed during the measurement (Fig. 1c), implying that the

377   particle composition was more affected by local emission or photochemical production than other

378   pathways. Organics showed a diurnal pattern with bimodal peaks respectively in the afternoon and

379   evening, which will be discussed later in section 3.3. The temporal profile of GF-PDF (Fig. 2)

380   measured by the H/V-TDMA was consistent with that of chemical composition, which showed a

381   significant diurnal pattern. This suggested that particles at all diameters could be affected by

382   atmospheric chemical processes and local emissions, which will be further discussed in section 3.3.

383   The H/V-TDMA data from 18th to 26th October and 29th October to 3rd November were not available

384   due to instrumental failure. In general, the GF-PDF exhibited a bimodal distribution for particles

385   larger than 30 nm, with a significant more-hygroscopic (MH, GF>1.33) or less-hygroscopic (LH,

386   1.11<GF<1.33) mode and a less obvious non-hygroscopic (NH, GF<1.11), indicating that these

387   particles were partly externally mixed. The NH mode with primary emissions (e.g., fresh black

388   carbon and some organics) was more obvious in a size range of 50-150 nm than others, suggesting

389   that these particles were more affected by local anthropogenic emissions. The above observation

390   was supported by the size distribution of the BC mass faction (Fig. S6), which peaked at a size range

391   of about 50-150 nm. Besides, the MH mode shifted to a higher GF value with an increase of particle

392   sizes, implying that larger particles were more aged with a higher fraction of inorganic salt (Fig. S6)

393   and well separated from the freshly emitted counterparts. A similar phenomenal pattern was

394   previously observed in the urban environment, including the PRD region (Hong et al., 2018;Cai et

395   al., 2017;Jiang et al., 2016;Tan et al., 2013b), the North China Plain (Liu et al., 2011;Ma et al., 2016)

396   and other city regions around the world (Yuan et al., 2020;Mochida et al., 2006;Massling et al.,

397   2005).

398   Table 3 summaries the N_{CCN}, activation ratio (AR), D_{50}, and κ_{CCN} values at 0.1%, 0.2%, 0.4%,

399   0.7%, 0.9%, and 1.0% SS during the campaign. The activation ratio is defined as the ratio of N_{CCN}

400   to N_{CN}, that is, $AR = N_{CCN}/N_{CN}$. The average N_{CCN} at 0.1%, 0.2%, 0.4%, 0.7%, 0.9%, and 1.0% SS

401   was about 2507, 4322, 5854, 6834, 7497, and 7862 cm^{-3}, respectively. The N_{CCN} at 0.7% SS was

402   lower than that measured (7900 cm^{-3} at 0.7% SS) in urban Guangzhou (Cai et al., 2018) and at a

403   suburban site (14400 cm^{-3} at 0.864% SS) in the North China Plain (Zhang et al., 2020), but

404   significantly higher than that measured at an urban site (2776 cm^{-3} at 0.68% SS) in São Paulo, Brazil

405   (Almeida et al., 2014). The average AR at the above six SS was 0.20, 0.34, 0.45, 0.52, 0.57, and

406   0.60, respectively. The AR at 0.7% SS was lower than the measured value (0.64 at 0.7% SS) in the

407   urban Guangzhou (Cai et al., 2018), while the corresponding D_{50} (52.56 nm) was lower than that

408   (58.45 nm) in the Guangzhou campaign, implying a higher CCN activity at this site. Thus, the lower

409   AR in this autumn campaign suggested that particles were more centered at smaller sizes, which

410 might be attributed to frequently occurred NPF at the Heshan site. The average κ values obtained

411 using HTDMA fall in a range of 0.1-0.17 at 30-200 nm (Fig. S7a), which were possibly attributed

412 to a high fraction of organic matter (Fig. S6). The κ_{AMS} is slightly higher than the κ_{HTDMA} and the

413 differences become larger with decreasing particle sizes. This was probably due to the overestimated

414 κ_{OA} at a small size range, which will be discussed in the next section. The hygroscopicity parameter

415 κ values obtained by the CCNc method were 0.48, 0.47, 0.31, 0.22, 0.20, and 0.20 at the above SS,

416 respectively, which were much higher than those measured by the HTDMA in this study. This

417 significant discrepancy between the measured κ_{CCN} and κ_{HTDMA} values might suggest that the water

418 uptake behavior is different under super- and sub-saturation condition, which is likely attributed to

419 the surfactant effect. It was reported that organic matter in the particles could serve as surfactant and

420 lower surface tension by about 0.01-0.032 N m^{-1}, leading to a higher CCN activity and thus a higher

421 κ_{CCN} (Petters and Kreidenweis, 2013; Ovadnevaite et al., 2017; Liu et al., 2018). According to Eqs.

422 (4) and (5), the κ_{CCN} was more susceptibly affected by the value of surface tension than that of

423 κ_{HTDMA}, which would lead to the discrepancy between κ_{CCN} and κ_{HTDMA} values. The surfactant effect

424 is closely related to the presence of liquid-liquid phase separation (LLPS) for organic-containing

425 particles at high RH (Renbaum-Wolff et al., 2016; Ruehl and Wilson, 2014). Once LLPS occurred,

426 the organic film on the droplet surface would decrease surface tension and enhance water uptake.

427 For particles of organic/inorganic mixture, the LLPS can occur when the O:C is lower than 0.8

428 (Bertram et al., 2011; Song et al., 2012a, b; Schill and Tolbert, 2013). The average O:C obtained

429 using AMS is about 0.53 in this campaign, suggesting that the LLPS likely occurred at

430 supersaturation conditions. Meanwhile, the variation of the discrepancy between κ_{CCN} and κ_{HTDMA}

431 is statistically insignificant during clean and polluted periods (Fig. S7b and S7c), implying that the

432 surfactant effect was hardly affected by pollution condition. Note that surface tension effect is not

433 the only factor which leads to a higher κ_{CCN}. It was found that κ_{CCN} could be higher than κ_{HTDMA},

434 since the existence of the slightly soluble compounds inhibits water uptake under subsaturation

435 conditions (Zhao et al., 2016; Pajunoja et al., 2015; Dusek et al., 2011; Petters et al., 2009; Hong et

436 al., 2014; Hansen et al., 2015). Other factors, such as different parameters used in the CCNc and

437 HTMDA calibration and function groups associated with the carbon chain, can lead to a gap between

438 κ_{HTDMA} and κ_{CCN} (Rose et al., 2008; Wex et al., 2009). More future work is needed to better

439 understand this water uptake mechanism and to improve the prediction of aerosol-cloud-climate

440 interactions.

441 **3.2 The average size-resolved hygroscopicity and volatility of OA**

442   The composition of organics could vary on a large scale with diameters due to different sources

443 and aging processes, which would further affect their properties. Figure 3 presents the average size-

444 resolved hygroscopicity and volatility of OA. The κ_{OA} values (vertical red lines in Fig. 3) ranged

445 from 0.058 to 0.09, within the range (0.05-0.15 at 100 nm) previously reported in the PRD region

446 (Hong et al., 2018) and slightly higher than that (0.03-0.06 at 250 nm) at a mountain site in Germany

447 (Wu et al., 2013). In general, the κ_{OA} values increased with particle sizes from 0.058 at 30 nm to

448 0.09 at 150 and 200 nm, similar to the feature observed in urban and forest environments (Kim et

449 al., 2020;Deng et al., 2019). The increases of the κ_{OA} values with particle sizes could be explained

450 by the oxidation level of organic aerosols (Massoli et al., 2010;Lambe et al., 2011;Xu et al., 2021).

451 Specifically, the hygroscopicity of OA was often found to be positively correlated to its oxidation

452 level (Mei et al., 2013;Lambe et al., 2011), which was usually represented by f_{44}, O/C ratio, or $\overline{OS_c}$.

453   Thus, the higher κ_{OA} values at larger particle diameters in this study might correspond to a higher

454   aging degree of these particles, and this was confirmed by the increasing trend of f_{44} with particle

455   diameters, i.e., the increasing fraction of CO_2^+ in OA in large particles (Fig. S8). Previous field

456   studies also indicated that f_{44} increased with particle diameters (Kim et al., 2020;Cai et al., 2018),

457   leading to a higher κ_{OA} value.

458   Besides the hygroscopicity of OA, we observed the size dependence of volatility. As shown in

459   Fig. 3, the mass fraction of ELVOA increases from 0.16 to 0.30 with the particle diameter, indicating

460   that the particles could be more aged at larger diameters, consistent with the higher κ_{OA} values as

461   discussed above. The ELVOA fraction in this campaign was higher than that in Beijing in summer

462   (0.13) measured by a thermodenuder (TD) coupled to an AMS (Xu et al., 2019), but similar to that

463   in Athens (0.3) using a similar TD system (Louvaris et al., 2017). The SVOA generally contributed

464   42%-57% to the OA at all measured sizes, comparable to the values reported in Centreville and

465   Raleigh (66-75%, Saha et al., 2017), Beijing (64%, Xu et al., 2019) and Mexico City (39%-73%,

466   Cappa and Jimenez, 2010). Note that the relationship between volatility and oxidation state of OA

467   is not usually strong. Saha et al. (2017) reported weak correlations (R < 0.3) between the mean

468   volatility ($\overline{C^*}$) and the mean oxidation state ($\overline{OS_C}$). Hong et al. (2017) also found that the volatility

469   distribution of OA derived from the combined V-TDMA and evaporation dynamic model could not

470   be fully explained by the organic factions determined by the PMF analysis based on the AMS data.

471   This is probably because the volatility was not only dependent on the $\overline{OS_C}$, but also the number of

472   atomic carbon (Donahue et al., 2011). In spite of this, the size-resolved volatility distribution can

473   provide a rough estimate of the aging degree of OA.

3.3 The diurnal variation of OA hygroscopicity and volatility

As discussed in Sect. 3.2, the hygroscopicity and volatility of OA could vary on a large range with particle diameters, which might be attributed to photochemical reactions and the OA sources. In this section, the diurnal variation of hygroscopicity and volatility of OA at different particle sizes was investigated, in combination with the PMF results. In general, the mass fraction of organics showed an obvious diurnal pattern during the whole campaign, with two peaks at about 14:00 and 19:00 LT (Fig. 4a), implying significant impacts of photochemical reactions and local emissions. Based on the PMF results (Fig. 5), the afternoon peak was attributed to secondary organics aerosol (SOA) formation (aBBOA and LOOA) during daytime, while the evening peak was explained by local residential activity (e.g., biomass burning and cooking, HOA and BBOA), as will be discussed later. A similar late-afternoon peak was observed in Hong Kong (Lee et al., 2013), where the OA enhancement was mainly contributed by traffic emissions. The f_{44} remained at a high level during daytime, consistent with strong photochemical reactions. A similar diurnal pattern was observed in the urban and sub-urban regions (Hong et al., 2018;Hu et al., 2016;Thalman et al., 2017), suggesting the consistent aging processes of pre-existing OA. In contrast, Deng et al. (2019) reported a relative low OA oxidation state during daytime in a forest environment, which could be explained by the SOA formation through photochemical oxidation of BVOCs.

The calculated κ_{HTDMA} and κ_{AMS} (the blue and red lines in Fig. 4b, respectively) values at 200 nm based on Eqs. (4) and (7) both reached minimum during daytime which was consistent with high OA fractions. This may be explained by lower hygroscopic of OA than inorganics as found in previous studies (Pajunoja et al., 2015;Zhao et al., 2015; Kuang et al., 2020b) as well as the low κ_i

495   values shown in Table 1. Although OA in a higher oxidation state could be hydrophilic (Massoli et

496   al., 2010), the primary OA is usually considered to be hydrophobic substance and their mixture

497   would be less hygroscopic (usually with average κ =0.1). The κ_{AMS} values were generally consistent

498   with those of the κ_{HTDMA} during daytime while the overestimated κ_{OA} was observed during nighttime.

499   This implies a lower κ_{OA} value than 0.1 at 200 nm during the nighttime, probably due to less

500   oxidation processes at night than those under the sunlight.

501   The average diurnal profile of PNSD is shown in Fig. 4c. Besides a stable accumulation mode

502   peaked at around 100 nm, a significantly growing mode of particle number from 20nm to 80 nm

503   was observed from 12:00 to 20:00 LT, which could be attributed to the frequently occurred NPF

504   during the campaign (Fig. 1a).

505   The size-resolved diurnal variations of κ_{OA} was explored in Fig. 6. Note that the κ_{OA} values are

506   presented in 2-hour resolution due to the low data coverage (Figs. 1 and 2). In general, a significantly

507   different pattern was observed between Aitken mode and accumulation mode. For Aitken mode

508   particles (30-100 nm), the κ_{OA} values were higher (0.05-0.1) before dawn than those (0.02-0.07)

509   during daytime, while this trend began to overturn at 150 and 200 nm, where the κ_{OA} values peaked

510   at noon (~0.09, Fig. 6). As reported in literature, the hygroscopicity of organics was partly dependent

511   on the aging degree (Liu et al., 2021;Zhao et al., 2016;Kim et al., 2020). The diurnal characteristics

512   of the size-resolved κ_{OA} indicate that the OA in small particles (30-100 nm) was fresh and became

513   aged in large particles. For the same campaign, Kuang et al. (2021) reported the bulk κ_{OA} of PM_1

514   based on aerosol optical hygroscopicity measurements, which could provide high time resolution

515   data of κ_{OA}. The relationship between κ_{OA} and different OA factors was investigated, which showed

516   a negative correlation (R=-0.25) between LOOA and κ_{OA}, while a positive correlation (R=0.35)

517   between aBBOA and κ_{OA}. Thus, the decrease of κ_{OA} for Aitken mode particles during daytime might

518   be attributed to the daytime formation of LOOA through gas-particle partitioning (Fig. 5). A similar

519   phenomenon was reported by Deng et al. (2019) in a forest environment, which might be attributed

520   to the photochemical reactions of BVOCs. Therefore, OA in small particles might be less aged and

521   was primarily contributed by photochemical oxidation of VOCs. In contrast, it is likely that the

522   accumulation mode particles became aged through photochemical oxidation during daylight, as

523   evidenced by higher fractions of ELVOA at 200 nm and higher κ_{OA} (Figs. 6 and 7) during daytime.

524   According to the PMF analysis, the daytime formation of aBBOA likely resulted from the aging

525   processes of primary OA or biomass burning related precursors (Fig. 5). As suggested by Kuang et

526   al. (2021), the daytime formation of aBBOA (Fig. 5) would lead to an increase of κ_{OA}, which likely

527   explained the noontime κ_{OA} peak at 150 and 200 nm. It suggested that the OA in the accumulation

528   mode was more influenced by the aging processes through photochemical reactions (leading to

529   aBBOA formation).

530   The average size-resolved volatility distribution of OA during daytime (8:00 to 16:00 LT) and

531   nighttime (20:00 to 4:00 LT) was demonstrated in Fig. 7. A higher fraction of semi-volatile organic

532   aerosol (SVOA) was observed at six measured sizes (30, 50, 80, 100, 150, and 200 nm) during

533   daytime. SVOA was usually related to primary emission (e.g., traffic, biomass burning) and gas-

534   particle partitioning (Donahue et al., 2012;Jathar et al., 2020;Hong et al., 2017; Saha et al., 2017).

535   Two primary emission factors, BBOA and HOA, remained at a relative low level during daytime,

536   suggesting that the higher fraction of SVOA during daylight might be more originated from gas-

537   particle partitioning. Note that gas-particle partitioning (leading to LOOA formation) could occur

538   at all measured diameters, as shown by the higher daytime fractions of SVOA (Fig. 7). In summary,

539   the above results indicate that the negative effect of LOOA on κ_{OA} might exist at all diameters, while

540   the positive effect of aBBOA was more dominant at larger particle sizes.

541   Meanwhile, the decreasing trend of κ_{OA} was observed from 18:00 to 24:00 at 80 and 100 nm

542   which might be related to the high mass fraction of OA from primary emissions (HOA and BBOA,

543   Fig. 5), owing to their hydrophobic nature. These two primary factors were associated with traffic

544   emissions, cooking and biomass burning. Zhang et al. (2005b) constructed the size distribution of

545   HOA based on the size-resolved m/z 44 and 57 from the AMS measurement and showed that HOA

546   was dominant ($\sim$75%) in ultrafine particles (D_{va}<100 nm). The size-resolved PMF results from Sun

547   et al. (2012) also indicated a high mass fraction of HOA (0.3-0.4) in Aitken mode particles. The

548   mass distribution of BC could be used to represent the distribution of primary OA (Cubison et al.,

549   2008;Wang et al., 2010;Zhang et al., 2005a) due to similar source origins for BC and HOA/BBOA.

550   The average mass fraction of BC peaked at about 80-100 nm (Fig. S6a), suggesting that HOA and

551   BBOA might be dominant at this size range. The BC peaks at 80 nm and 100 nm were consistent

552   with those of the SVOA mass fraction (Fig. 3), which was attributed to biomass burning as similar

553   characteristics for the BC peak were shown in other studies (May et al., 2013;Huffman et al.,

554   2009;Donahue et al., 2011). Furthermore, this conclusion was supported by the hygroscopicity

555   measurements as a significant NH mode for 80-100 nm particles was found (Fig. 2). Overall, these

556   results highlight that the diurnal variation of physicochemical properties of OA could vary in a large

557   range with particle diameters, and further investigation is needed.

558   **3.4 Implication for CCN activity**

559   The CCN activity and its prediction is essential in global climate model and evaluation. A κ_{OA}

560   value of 0.1~0.15 was widely adopted in the prediction of N_{CCN} based on aerosol chemical

561   composition (Meng et al., 2014;Wang et al., 2010;Almeida et al., 2014). As discussed in Sect. 3.3,

562   the κ_{OA} values might be dependent on particle sizes and vary diurnally, which in turn affect N_{CCN}.

563   Here, different κ_{OA} values were adopted to predict N_{CCN} and the impact of κ_{OA} on N_{CCN} was

564   investigated through comparison between the predicted and measured N_{CCN}. Note that we only

565   discussed the N_{CCN} at 0.1%, 0.2%, 0.4% and 0.7% SS, since the D_{50} at higher SS (0.9% and 1.0%)

566   was within a narrow range (35-60 nm).

567   The N_{CCN} at a certain SS can be calculated using PNSD and D_{50}:

568    $$N_{CCN,p}(SS) = \int_{D_{50}}^{\infty} n_i dlogDp_i \tag{16}$$

569   where n_i is the particle distribution function at Dp_i and D_{50} is determined from the κ_{AMS} using Eqs.

570   (5) and (7). The D_{50} at 0.1%, 0.2%, 0.4% and 0.7% SS ranged from about 130-160 nm, 90-110 nm,

571   60-80 nm and 45-60 nm, respectively. Three κ_{OA} schemes were proposed to predict N_{CCN}: (1) fixed

572   κ_{OA}, where κ_{OA} was assumed to be 0.1 for all size particles. (2) size-resolved κ_{OA} (SR κ_{OA}), where

573   κ_{OA} was taken from average size-resolved κ_{OA} (κ_{OA} at 50, 80, 100 and 150 nm for 0.7%, 0.4%, 0.2%

574   and 0.1% SS, respectively) in Sect. 3.2. (3) size-resolved diurnal κ_{OA} (SR diurnal κ_{OA}), where κ_{OA}

575   was the average diurnal value of κ_{OA} at each diameter (κ_{OA} at 50, 80, 100 and 150 nm for 0.7%,

576   0.4%, 0.2% and 0.1% SS, respectively) as shown in Sect. 3.3. The κ_{AMS} was calculated based on the

577   chemical composition at the corresponding D_{50} range. Note that the N_{CCN} prediction based on the

578   SR diurnal κ_{OA} scheme was presented in 2 h time resolution and the particles were assumed to be

579   internally mixed in Eq. (16). The internal mixing assumption could slightly increase the predicted

580   N_{CCN} by about 6-10% (Sect. S3). As aforementioned, organics can increase the CCN activity by

581   decreasing surface tension, which might lead to significant discrepancy between κ_{HTDMA} and κ_{CCN}

582 in this campaign (Fig. S7). In addition, this effect could result in a significant underestimation of

583 N_{CCN} (Ovadnevaite et al., 2017;Liu et al., 2018;Good et al., 2010; Noziere, 2016).

584 Here, we evaluate the surface tension effect by comparing κ_{HTDMA} and κ_{CCN} as a function of

585 $\sigma_{s/a}$ (Fig. S9). The κ_{CCN} reached κ_{HTDMA} when the $\sigma_{s/a}$ values were set to be about 0.059 N m^{-1} at

586 0.7%, 0.9% and 1.0% SS, 0.053 N m^{-1} at 0.4% SS, 0.047 N m^{-1} at 0.2% SS, and 0.049 N m^{-1} at 0.1%

587 SS, respectively. Thus, we adopted $\sigma_{s/a}$ values of 0.049, 0.047, 0.053 and 0.059 N m^{-1} to predict

588 N_{CCN} at 0.1%, 0.2%, 0.4% and 0.7% SS, respectively. In general, the N_{CCN} prediction could be

589 significantly improved by considering the surfactant effect (Fig. S10). The N_{CCN} was slightly

590 overestimated by using reduced $\sigma_{s/a}$ values, which was probably due to using a fixed κ_{OA} values.

591 This bias could be corrected by adopting SR κ_{OA} scheme (Fig. S11).

592 The deviation of the N_{CCN} prediction ($\delta_{N_{CCN}}$) at a certain SS is defined as (Cai et al., 2021b):

593 $$\delta_{N_{CCN}}(SS) = \frac{N_{CCN,m}(SS) - N_{CCN,p}(SS)}{N_{CCN,m}(SS)} 100\% \tag{17}$$

594 where $N_{CCN,m}(SS)$ is the measured N_{CCN} at a specific SS. A negative $\delta_{N_{CCN}}$ indicates an

595 overestimate of N_{CCN}, and vice versa.

596 Figure 8 shows the $\delta_{N_{CCN}}$ at different SS for the three κ_{OA} schemes. Fixed κ_{OA} scheme gave

597 generally a negative value of $\delta_{N_{CCN}}$ (-0.18 to -0.02) at 0.7% SS, indicating an N_{CCN} overestimation,

598 due to lower κ_{OA} values for smaller particles. A significant diurnal pattern of $\delta_{N_{CCN}}$ was observed at

599 all SS. The $\delta_{N_{CCN}}$ was relatively higher during daytime at 0.1% SS, while an opposite pattern was

600 shown at high SS, consistent with the size-dependent variation of κ_{OA} (Fig. 6). Hence, the fixed κ_{OA}

601 scheme could lead to an obvious discrepancy in the N_{CCN} prediction as SS increased. The results

602 based on the SR κ_{OA} scheme showed that the minimum $\delta_{N_{CCN}}$ value at 0.7% SS increased from -

603 0.18 in the fixed κ_{OA} scheme to -0.08, indicating the improvement for the N_{CCN} prediction at high

604   SS (Fig. 8b). However, only minor improvement was observed at SS lower than 0.4 % because of

605   the low employed κ_{OA} (about 0.08), which was close to the κ_{OA} value (0.1) adopted in the fixed κ_{OA}

606   scheme. A significant difference of $\delta_{N_{CCN}}$ was still observed in the diurnal pattern at high and low

607   SS, implying the impact of the diurnal variation of κ_{OA} on the N_{CCN} prediction. To further investigate

608   this impact, the SR diurnal κ_{OA} scheme was employed to calculate $\delta_{N_{CCN}}$ and the results were shown

609   in Fig. 8c. The $\delta_{N_{CCN}}$ value at 0.7% SS varied from -0.04 to 0.09 with an average value of 0, whereas

610   it ranged from 0 to 0.11 at 0.1% SS. Hence, the discrepancies of $\delta_{N_{CCN}}$ among different SS became

611   minor compared to the other two schemes as a relatively flat diurnal pattern of $\delta_{N_{CCN}}$ was observed

612   at all SS. It implies that better prediction of N_{CCN} could be achieved by considering the diurnal

613   variation and the size dependence of κ_{OA}.

614   **4.   Conclusions**

615   A rural field measurement was conducted at the Heshan supersite in the PRD region of China

616   during October and November 2019. We investigated the diurnal variation and size dependence in

617   the hygroscopicity and volatility of OA in combination with the PMF analysis of the AMS data. The

618   impacts of OA on the CCN number concentration at different SS were discussed for various given

619   size-dependent κ_{OA} values.

620   In general, the average κ_{OA} values varied from 0.058 at 30 nm to 0.09 at 200 nm, indicating a

621   higher oxidation degree of OA at larger sizes than at smaller sizes. This is consistent with particle

622   volatility: the mass fraction of ELVOA increased (0.16-0.30) with increasing particle diameters.

623   Our results suggest that the formation and aging processes of OA might vary with particle sizes.

624 An oppositely diurnal pattern of κ_{OA} was observed between Aitken mode (30-100 nm) and

625 Accumulation mode (150 and 200 nm) particles, suggesting different atmospheric evolution

626 processes of OA at different diameters. The gas-particle partitioning could decrease the κ_{OA}, while

627 the aging processes of preexisting particles could enhance the hygroscopicity of OA. For Aitken

628 mode particles (30-100 nm), the κ_{OA} values reached minimal (0.02-0.07) during daytime.

629 Meanwhile, a daytime peak was observed for the κ_{OA} value (~0.09) in the accumulation mode (150

630 and 200 nm), suggesting that the aging processes of preexisting particles were more dominant at

631 accumulation mode particles. In addition, the mass faction of SVOA was higher during daytime at

632 all measured diameters, implying that the formation of LOOA through gas-particle partitioning was

633 independent of particle diameters.

634 The impact of the size-resolved diurnal variation of κ_{OA} on the N_{CCN} was investigated. The use

635 of fixed κ_{OA} (κ_{OA}=0.1) overestimated the N_{CCN} up to 18% at 0.7% SS. The diurnal deviation became

636 obvious at 0.7% SS and minor at 0.1% SS during daytime, owing to the size-dependent variation of

637 κ_{OA}. The N_{CCN} prediction at 0.7% SS was improved if the SR κ_{OA} scheme was used, while the

638 diurnal variation of $\delta_{N_{CCN}}$ still existed. Better predictions can be obtained by using SR diurnal κ_{OA}.

639 Our results highlight that the physical properties of OA can vary in a large range at different size

640 ranges due to the formation and aging processes, and the size-resolved diurnal variation in κ_{OA} plays

641 an important role in the N_{CCN} prediction at different SS. Further studies on the size-resolved

642 physicochemical properties of OA should be performed in different environments to better

643 understand their impact on cloud formation and hence climate.

644

645 *Data   availability.*   Data   from   the   measurements   are   available   at

646 https://doi.org/10.6084/m9.figshare.18094277.v1 (Cai et al., 2022).

647

648 *Supplement.* The supplement related to this article is available online at xxx.

649

650 *Author contributions.* **MC, SH, BY and LL** designed the research. **MC**, **SH, MS, BY, YP, ZW, DC,**

651 **WC, QS, WL, BL and QS** performed the measurements. **MC, SH, BL, QS, LL, BY, WH, WC,**

652 **QS, WL, YP, ZW, HT, HX, FL, DX, TD, JS and JZ** analyzed the data. **MC, SH** and **LL** wrote the

653 paper with contributions from all co-authors.

654

655 *Competing interests.* The authors declare that they have no conflict of interest.

656

657 *Financial support.* This work was supported by the Key-Area Research and Development Program

658 of Guangdong Province (grant no. 2019B110206001), the National Key R&D Plan of China (grant

659 no. 2019YFE0106300 and 2018YFC0213904), the National Natural Science Foundation of China

660 (grant nos. 41877302, 91644225, 41775117 and 41807302), Guangdong Natural Science Funds for

661 Distinguished Young Scholar (grant no. 2018B030306037), Guangdong Innovative and

662 Entrepreneurial Research Team Program (grant no. 2016ZT06N263), Guangdong Province Key

663 Laboratory for Climate Change and Natural Disaster Studies (grant no. 2020B1212060025),

664 Guangdong Basic and Applied Basic Research Foundation (grant nos. 2019A1515110790 and

665 2019A1515110791), Science and Technology Research project of Guangdong Meteorological

666 Bureau (grant no. GRMC2018M07), the Natural Science Foundation of Guangdong Province,

667 China (grant no. 2016A030311007), Science and Technology Innovation Team Plan of Guangdong

668   Meteorological Bureau (grant no. GRMCTD202003), and Science and Technology Program of

669   Guangdong Province (Science and Technology Innovation Platform Category, No.

670   2019B121201002).

671

672   *Acknowledgements.* Additional support from the crew of the Heshan supersite and Guangdong

673   Environmental Monitoring Center is greatly acknowledged.

674

675   **References**

676   Almeida, G. P., Brito, J., Morales, C. A., Andrade, M. F., and Artaxo, P.: Measured and

677   modelled cloud condensation nuclei (CCN) concentration in São Paulo, Brazil: the importance of

678   aerosol size-resolved chemical composition on CCN concentration prediction, Atmos. Chem. Phys.,

679   14, 7559-7572, 10.5194/acp-14-7559-2014, 2014.

680   Bertram, A. K., Martin, S. T., Hanna, S. J., Smith, M. L., Bodsworth, A., Chen, Q., Kuwata, M., Liu,

681   A., You, Y., and Zorn, S. R.: Predicting the relative humidities of liquid-liquid phase separation,

682   efflorescence, and deliquescence of mixed particles of ammonium sulfate, organic material, and water

683   using the organic-to-sulfate mass ratio of the particle and the oxygen-to-carbon elemental ratio of the

684   organic component, Atmos. Chem. Phys., 11, 10995-11006, 10.5194/acp-11-10995-2011, 2011.

685   Cai, J., Chu, B., Yao, L., Yan, C., Heikkinen, L. M., Zheng, F., Li, C., Fan, X., Zhang, S., Yang,

686   D., Wang, Y., Kokkonen, T. V., Chan, T., Zhou, Y., Dada, L., Liu, Y., He, H., Paasonen, P., Kujansuu,

687   J. T., Petäjä, T., Mohr, C., Kangasluoma, J., Bianchi, F., Sun, Y., Croteau, P. L., Worsnop, D. R.,

688   Kerminen, V. M., Du, W., Kulmala, M., and Daellenbach, K. R.: Size-segregated particle number

689   and mass concentrations from different emission sources in urban Beijing, Atmos. Chem. Phys., 20,

690   12721-12740, 10.5194/acp-20-12721-2020, 2020.

691   Cai, M., Huang, S., Li, L., Yuan, B., Shao, M., and Zhao, J.: Distinct size dependence and

692   diurnal variation of OA hygroscopicity, volatility, and CCN activity at a rural site in the Pearl River

693   Delta (PRD) region, China. figshare. Dataset., https://doi.org/10.6084/m9.figshare.18094277.v1,

694   2022.

695   Cai, M., Tan, H., Chan, C. K., Mochida, M., Hatakeyama, S., Kondo, Y., Schurman, M. I., Xu,

696   H., Li, F., and Shimada, K.: Comparison of Aerosol Hygroscopcity, Volatility, and Chemical

697   Composition between a Suburban Site in the Pearl River Delta Region and a Marine Site in Okinawa,

698   Aerosol Air Qual. Res., 2017.

699   Cai, M., Tan, H., Chan, C. K., Qin, Y., Xu, H., Li, F., Schurman, M. I., Liu, L., and Zhao, J.:

700   The size-resolved cloud condensation nuclei (CCN) activity and its prediction based on aerosol

701   hygroscopicity and composition in the Pearl Delta River (PRD) region during wintertime 2014,

702   Atmos. Chem. Phys., 18, 16419-16437, 2018.

703   Cai, M., Liang, B., Sun, Q., Liu, L., Yuan, B., Shao, M., Huang, S., Peng, Y., Wang, Z., Tan,

704   H., Li, F., Xu, H., Chen, D., and Zhao, J.: The important roles of surface tension and growth rate in

705   the contribution of new particle formation (NPF) to cloud condensation nuclei (CCN) number

706   concentration: evidence from field measurements in southern China, Atmos. Chem. Phys., 21, 8575-

707   8592, 10.5194/acp-21-8575-2021, 2021a.

708   Cai, M. F., Liang, B. L., Sun, Q. B., Zhou, S. Z., Yuan, B., Shao, M., Tan, H. B., Xu, Y. S., Ren,

709   L. H., and Zhao, J.: Contribution of New Particle Formation to Cloud Condensation Nuclei Activity

710   and its Controlling Factors in a Mountain Region of Inland China, J. Geophys. Res. Atmos., 126,

711   e2020JD034302, https://doi.org/10.1029/2020JD034302, 2021b.

712   Canagaratna, M. R., Jayne, J. T., Jimenez, J. L., Allan, J. D., Alfarra, M. R., Zhang, Q., Onasch,

713   T. B., Drewnick, F., Coe, H., Middlebrook, A., Delia, A., Williams, L. R., Trimborn, A. M.,

714   Northway, M. J., DeCarlo, P. F., Kolb, C. E., Davidovits, P., and Worsnop, D. R.: Chemical and

715   microphysical characterization of ambient aerosols with the aerodyne aerosol mass spectrometer,

716   Mass Spectrom. Rev., 26, 185-222, 10.1002/mas.20115, 2007.

717   Cappa, C. D., and Jimenez, J. L.: Quantitative estimates of the volatility of ambient organic

718   aerosol, Atmos. Chem. Phys., 10, 5409-5424, 10.5194/acp-10-5409-2010, 2010.

719   Chang, R. Y. W., Slowik, J. G., Shantz, N. C., Vlasenko, A., Liggio, J., Sjostedt, S. J., Leaitch,

720   W. R., and Abbatt, J. P. D.: The hygroscopicity parameter (κ) of ambient organic aerosol at a field

721   site subject to biogenic and anthropogenic influences: relationship to degree of aerosol oxidation,

722   Atmos. Chem. Phys.,10,11(2010-06-01), 10, 5047-5064, 2010.

723   Chen, C., Sun, Y. L., Xu, W. Q., Du, W., Zhou, L. B., Han, T. T., Wang, Q. Q., Fu, P. Q., Wang,

724   Z. F., Gao, Z. Q., Zhang, Q., and Worsnop, D. R.: Characteristics and sources of submicron aerosols

725   above the urban canopy (260 m) in Beijing, China, during the 2014 APEC summit, Atmos. Chem.

726   Phys., 15, 12879-12895, 10.5194/acp-15-12879-2015, 2015.

727   Chen, J., Budisulistiorini, S. H., Itoh, M., Lee, W. C., Miyakawa, T., Komazaki, Y., Yang, L. D.

728   Q., and Kuwata, M.: Water uptake by fresh Indonesian peat burning particles is limited by water-

729   soluble organic matter, Atmos. Chem. Phys., 17, 11591-11604, 10.5194/acp-17-11591-2017, 2017.

730   Cheung, H. H., Tan, H., Xu, H., Li, F., Wu, C., Yu, J. Z., and Chan, C. K.: Measurements of

731   non-volatile aerosols with a VTDMA and their correlations with carbonaceous aerosols in

732   Guangzhou, China, Atmos. Chem. Phys., 16, 8431-8446, 2016.

733   Cubison, M. J., Ervens, B., Feingold, G., Docherty, K. S., Ulbrich, I. M., Shields, L., Prather,

734   K., Hering, S., and Jimenez, J. L.: The influence of chemical composition and mixing state of Los

735   Angeles urban aerosol on CCN number and cloud properties, Atmos. Chem. Phys., 8, 5649-5667,

736   10.5194/acp-8-5649-2008, 2008.

737   Deng, Y., Kagami, S., Ogawa, S., Kawana, K., Nakayama, T., Kubodera, R., Adachi, K.,

738   Hussein, T., Miyazaki, Y., and Mochida, M.: Hygroscopicity of Organic Aerosols and Their

739   Contributions to CCN Concentrations Over a Midlatitude Forest in Japan, J. Geophys. Res. Atmos.,

740   123, 9703-9723, 10.1029/2017JD027292, 2018.

741   Deng, Y., Yai, H., Fujinari, H., Kawana, K., Nakayama, T., and Mochida, M.: Diurnal variation

742   and size dependence of the hygroscopicity of organic aerosol at a forest site in Wakayama, Japan:

743   their relationship to CCN concentrations, Atmos. Chem. Phys., 19, 5889-5903, 10.5194/acp-19-

744   5889-2019, 2019.

745   Donahue, N. M., Epstein, S. A., Pandis, S. N., and Robinson, A. L.: A two-dimensional

746   volatility basis set: 1. organic-aerosol mixing thermodynamics, Atmos. Chem. Phys., 11, 3303-3318,

747   10.5194/acp-11-3303-2011, 2011.

748   Donahue, N. M., Kroll, J. H., Pandis, S. N., and Robinson, A. L.: A two-dimensional volatility

749   basis set – Part 2: Diagnostics of organic-aerosol evolution, Atmos. Chem. Phys., 12, 615-634,

750   10.5194/acp-12-615-2012, 2012.

751   Dusek, U., Frank, G. P., Massling, A., Zeromskiene, K., Iinuma, Y., Schmid, O., Helas, G.,

752 Hennig, T., Wiedensohler, A., and Andreae, M. O.: Water uptake by biomass burning aerosol at sub-

753 and supersaturated conditions: closure studies and implications for the role of organics, Atmos.

754 Chem. Phys., 11, 9519-9532, 10.5194/acp-11-9519-2011, 2011.

755   Engelhart, G. J., Moore, R. H., Nenes, A., and Pandis, S. N.: Cloud condensation nuclei activity

756 of isoprene secondary organic aerosol, J. Geophys. Res. Atmos., 116,

757 https://doi.org/10.1029/2010JD014706, 2011.

758   Epstein, S. A., Riipinen, I., and Donahue, N. M.: A Semiempirical Correlation between

759 Enthalpy of Vaporization and Saturation Concentration for Organic Aerosol, Environ. Sci. Technol.,

760 44, 743-748, 10.1021/es902497z, 2010.

761   Gantt, B., and Meskhidze, N.: The physical and chemical characteristics of marine primary

762 organic aerosol: a review, Atmos. Chem. Phys., 13, 3979-3996, 10.5194/acp-13-3979-2013, 2013.

763   Good, N., Topping, D., Allan, J., Flynn, M., Fuentes, E., Irwin, M., Williams, P., Coe, H., and

764 McFiggans, G.: Consistency between parameterisations of aerosol hygroscopicity and CCN activity

765 during the RHaMBLe discovery cruise, Atmos. Chem. Phys., 10, 3189-3203, 2010.

766   Guo, J., Zhou, S., Cai, M., Zhao, J., Song, W., Zhao, W., Hu, W., Sun, Y., He, Y., Yang, C., Xu,

767 X., Zhang, Z., Cheng, P., Fan, Q., Hang, J., Fan, S., Wang, X., and Wang, X.: Characterization of

768 submicron particles by time-of-flight aerosol chemical speciation monitor (ToF-ACSM) during

769 wintertime: aerosol composition, sources, and chemical processes in Guangzhou, China, Atmos.

770 Chem. Phys., 20, 7595-7615, 10.5194/acp-20-7595-2020, 2020.

771   Gysel, M., Crosier, J., Topping, D. O., Whitehead, J. D., Bower, K. N., Cubison, M. J., Williams,

772 P. I., Flynn, M. J., McFiggans, G. B., and Coe, H.: Closure study between chemical composition

773 and hygroscopic growth of aerosol particles during TORCH2, Atmos. Chem. Phys., 7, 6131-6144,

774 10.5194/acp-7-6131-2007, 2007.

775   Hallquist, M., Wenger, J. C., Baltensperger, U., Rudich, Y., Simpson, D., Claeys, M., Dommen,

776 J., Donahue, N., George, C., and Goldstein, A.: The formation, properties and impact of secondary

777 organic aerosol: current and emerging issues, Atmospheric chemistry and physics, 9, 5155-5236,

778 2009.

779   Hansen, A. M. K., Hong, J., Raatikainen, T., Kristensen, K., Ylisirniö, A., Virtanen, A., Petäjä, T.,

780 Glasius, M., and Prisle, N. L.: Hygroscopic properties and cloud condensation nuclei activation of

781 limonene-derived organosulfates and their mixtures with ammonium sulfate, Atmos. Chem. Phys., 15,

782 14071-14089, 10.5194/acp-15-14071-2015, 2015.

783 Hersey, S. P., Craven, J. S., Metcalf, A. R., Lin, J., Lathem, T., Suski, K. J., Cahill, J. F., Duong, H.

784 T., Sorooshian, A., Jonsson, H. H., Shiraiwa, M., Zuend, A., Nenes, A., Prather, K. A., Flagan, R. C., and

785 Seinfeld, J. H.: Composition and hygroscopicity of the Los Angeles Aerosol: CalNex, Journal of

786 Geophysical Research: Atmospheres, 118, 3016-3036, https://doi.org/10.1002/jgrd.50307, 2013.

787 Hong, J., Äijälä, M., Häme, S. A. K., Hao, L., Duplissy, J., Heikkinen, L. M., Nie, W., Mikkilä,

788 J., Kulmala, M., Prisle, N. L., Virtanen, A., Ehn, M., Paasonen, P., Worsnop, D. R., Riipinen, I.,

789 Petäjä, T., and Kerminen, V. M.: Estimates of the organic aerosol volatility in a boreal forest using

790 two independent methods, Atmos. Chem. Phys., 17, 4387-4399, 10.5194/acp-17-4387-2017, 2017.

791 Hong, J., Xu, H., Tan, H., Yin, C., Hao, L., Li, F., Cai, M., Deng, X., Wang, N., Su, H., Cheng,

792 Y., Wang, L., Petäjä, T., and Kerminen, V. M.: Mixing state and particle hygroscopicity of organic-

793 dominated aerosols over the Pearl River Delta region in China, Atmos. Chem. Phys., 18, 14079-

794 14094, 10.5194/acp-18-14079-2018, 2018.

795 Hong, J., Häkkinen, S. A. K., Paramonov, M., Äijälä, M., Hakala, J., Nieminen, T., Mikkilä, J.,

796 Prisle, N. L., Kulmala, M., Riipinen, I., Bilde, M., Kerminen, V. M., and Petäjä, T.: Hygroscopicity, CCN

797 and volatility properties of submicron atmospheric aerosol in a boreal forest environment during the

798 summer of 2010, Atmos. Chem. Phys., 14, 4733-4748, 10.5194/acp-14-4733-2014, 2014.Hu, W., Hu,

799 M., Hu, W., Jimenez, J. L., Yuan, B., Chen, W., Wang, M., Wu, Y., Chen, C., Wang, Z., Peng, J.,

800 Zeng, L., and Shao, M.: Chemical composition, sources, and aging process of submicron aerosols

801 in Beijing: Contrast between summer and winter, J. Geophys. Res. Atmos., 121, 1955-1977,

802 https://doi.org/10.1002/2015JD024020, 2016.

803 Huang, R.-J., Zhang, Y., Bozzetti, C., Ho, K.-F., Cao, J.-J., Han, Y., Daellenbach, K. R., Slowik,

804 J. G., Platt, S. M., and Canonaco, F.: High secondary aerosol contribution to particulate pollution

805 during haze events in China, Nature, 514, 218, 2014.

806 Huang, S., Wu, Z., Poulain, L., van Pinxteren, M., Merkel, M., Assmann, D., Herrmann, H.,

807 and Wiedensohler, A.: Source apportionment of the organic aerosol over the Atlantic Ocean from

808 53°N to 53°S: significant contributions from marine emissions and long-range transport, Atmos.

809   Chem. Phys., 18, 18043-18062, 10.5194/acp-18-18043-2018, 2018.

810   Huffman, J. A., Docherty, K. S., Aiken, A. C., Cubison, M. J., Ulbrich, I. M., DeCarlo, P. F.,

811   Sueper, D., Jayne, J. T., Worsnop, D. R., Ziemann, P. J., and Jimenez, J. L.: Chemically-resolved

812   aerosol volatility measurements from two megacity field studies, Atmos. Chem. Phys., 9, 7161-

813   7182, 10.5194/acp-9-7161-2009, 2009.

814   Jathar, S. H., Sharma, N., Galang, A., Vanderheyden, C., Takhar, M., Chan, A. W. H., Pierce, J.

815   R., and Volckens, J.: Measuring and modeling the primary organic aerosol volatility from a modern

816   non-road diesel engine, Atmos. Environ., 223, 117221,

817   https://doi.org/10.1016/j.atmosenv.2019.117221, 2020.

818   Jiang, R., Tan, H., Tang, L., Cai, M., Yin, Y., Li, F., Liu, L., Xu, H., Chan, P. W., and Deng, X.:

819   Comparison of aerosol hygroscopicity and mixing state between winter and summer seasons in Pearl

820   River Delta region, China, Atmos. Res., 169, 160-170, 2016.

821   Jimenez, J. L., Canagaratna, M., Donahue, N., Prevot, A., Zhang, Q., Kroll, J. H., DeCarlo, P.

822   F., Allan, J. D., Coe, H., and Ng, N.: Evolution of organic aerosols in the atmosphere, Science, 326,

823   1525-1529, 2009.

824   Kanakidou, M., Seinfeld, J., Pandis, S., Barnes, I., Dentener, F., Facchini, M., Dingenen, R. V.,

825   Ervens, B., Nenes, A., and Nielsen, C.: Organic aerosol and global climate modelling: a review,

826   Atmos. Chem. Phys., 5, 1053-1123, 2005.

827   Kim, N., Yum, S. S., Park, M., Park, J. S., Shin, H. J., and Ahn, J. Y.: Hygroscopicity of urban

828   aerosols and its link to size-resolved chemical composition during spring and summer in Seoul,

829   Korea, Atmos. Chem. Phys., 20, 11245-11262, 10.5194/acp-20-11245-2020, 2020.

830   Kiyoura, R., and Urano, K.: Mechanism, Kinetics, and Equilibrium of Thermal Decomposition

831   of Ammonium Sulfate, Ind. Eng. Chem. Process Des. Dev. , 9, 489-494, 10.1021/i260036a001,

832   1970.

833   Kuang, Y., He, Y., Xu, W., Yuan, B., Zhang, G., Ma, Z., Wu, C., Wang, C., Wang, S., Zhang,

834   S., Tao, J., Ma, N., Su, H., Cheng, Y., Shao, M., and Sun, Y.: Photochemical Aqueous-Phase

835   Reactions Induce Rapid Daytime Formation of Oxygenated Organic Aerosol on the North China

836   Plain, Environ. Sci. Technol., 54, 3849-3860, 10.1021/acs.est.9b06836, 2020a.

837   Kuang, Y., Xu, W., Tao, J., Ma, N., Zhao, C., and Shao, M.: A Review on Laboratory Studies

838 and Field Measurements of Atmospheric Organic Aerosol Hygroscopicity and Its Parameterization

839 Based on Oxidation Levels, Curr. Pollut. Rep., 10.1007/s40726-020-00164-2, 2020b.

840 Kuang, Y., Huang, S., Xue, B., Luo, B., Song, Q., Chen, W., Hu, W., Li, W., Zhao, P., Cai, M.,

841 Peng, Y., Qi, J., Li, T., Wang, S., Chen, D., Yue, D., Yuan, B., and Shao, M.: Contrasting effects of

842 secondary organic aerosol formations on organic aerosol hygroscopicity, Atmos. Chem. Phys., 21,

843 10375-10391, 10.5194/acp-21-10375-2021, 2021.

844 Lambe, A. T., Onasch, T. B., Massoli, P., Croasdale, D. R., Wright, J. P., Ahern, A. T., Williams,

845 L. R., Worsnop, D. R., Brune, W. H., and Davidovits, P.: Laboratory studies of the chemical

846 composition and cloud condensation nuclei (CCN) activity of secondary organic aerosol (SOA) and

847 oxidized primary organic aerosol (OPOA), Atmos. Chem. Phys., 11, 8913-8928, 10.5194/acp-11-

848 8913-2011, 2011.

849 Lee, B.-H., Kostenidou, E., Hildebrandt, L., Riipinen, I., Engelhart, G., Mohr, C., DeCarlo, P.,

850 Mihalopoulos, N., Prevot, A., Baltensperger, U.: Measurement of the ambient organic aerosol

851 volatility distribution: application during the Finokalia Aerosol Measurement Experiment (FAME-

852 2008), Atmos. Chem. Phys., 10, 12149-12160, 2010.

853 Lee, B.-H., Pierce, J. R., Engelhart, G. J., and Pandis, S. N.: Volatility of secondary organic

854 aerosol from the ozonolysis of monoterpenes, Atmos. Environ., 45, 2443-2452, 2011.

855 Lee, B. P., Li, Y. J., Yu, J. Z., Louie, P. K., and Chan, C. K.: Physical and chemical

856 characterization of ambient aerosol by HR-ToF-AMS at a suburban site in Hong Kong during

857 springtime 2011, J. Geophys. Res. Atmos., 118, 8625-8639, 2013.

858 Li, J., Wang, G., Zhou, B., Cheng, C., Cao, J., Shen, Z., and An, Z.: Airborne particulate

859 organics at the summit (2060m, a.s.l.) of Mt. Hua in central China during winter: Implications for

860 biofuel and coal combustion, Atmos. Res., 106, 108-119,

861 https://doi.org/10.1016/j.atmosres.2011.11.012, 2012.

862 Li, Y. J., Lee, B., Yu, J., Ng, N., and Chan, C. K.: Evaluating the degree of oxygenation of

863 organic aerosol during foggy and hazy days in Hong Kong using high-resolution time-of-flight

864 aerosol mass spectrometry (HR-ToF-AMS), Atmos. Chem. Phys., 13, 8739-8753, 2013.

865 Liu, J., Zhang, F., Xu, W., Sun, Y., Chen, L., Li, S., Ren, J., Hu, B., Wu, H., and Zhang, R.:

866 Hygroscopicity of Organic Aerosols Linked to Formation Mechanisms, Geophys. Res. Lett., 48,

867   e2020GL091683, https://doi.org/10.1029/2020GL091683, 2021.

868   Liu, P., Song, M., Zhao, T., Gunthe, S. S., Ham, S., He, Y., Qin, Y. M., Gong, Z., Amorim, J.

869   C., Bertram, A. K., and Martin, S. T.: Resolving the mechanisms of hygroscopic growth and cloud

870   condensation nuclei activity for organic particulate matter, Nat. Commun., 9, 4076,

871   10.1038/s41467-018-06622-2, 2018.

872   Liu, P. F., Zhao, C. S., Göbel, T., Hallbauer, E., Nowak, A., Ran, L., Xu, W. Y., Deng, Z. Z.,

873   Ma, N., Mildenberger, K., Henning, S., Stratmann, F., and Wiedensohler, A.: Hygroscopic properties

874   of aerosol particles at high relative humidity and their diurnal variations in the North China Plain,

875   Atmos. Chem. Phys., 11, 3479-3494, 10.5194/acp-11-3479-2011, 2011.

876   Liu, X., and Wang, J.: How important is organic aerosol hygroscopicity to aerosol indirect

877   forcing?, Environ. Res. Lett., 5, 044010, 10.1088/1748-9326/5/4/044010, 2010.

878   Louvaris, E. E., Florou, K., Karnezi, E., Papanastasiou, D. K., Gkatzelis, G. I., and Pandis, S.

879   N.: Volatility of source apportioned wintertime organic aerosol in the city of Athens, Atmos.

880   Environ., 158, 138-147, https://doi.org/10.1016/j.atmosenv.2017.03.042, 2017.

881   Noziere, B.: Don't forget the surface, Science, 351, 1396-1397, 10.1126/science.aaf3253, 2016.

882   Ma, N., Zhao, C., Tao, J., Wu, Z., Kecorius, S., Wang, Z., Größ, J., Liu, H., Bian, Y., and Kuang,

883   Y.: Variation of CCN activity during new particle formation events in the North China Plain, Atmos.

884   Chem. Phys., 16, 8593-8607, 2016.

885   Massling, A., Stock, M., and Wiedensohler, A.: Diurnal, weekly, and seasonal variation of

886   hygroscopic properties of submicrometer urban aerosol particles, Atmos. Environ., 39, 3911-3922,

887   10.1016/j.atmosenv.2005.03.020, 2005.

888   Massoli, P., Lambe, A., Ahern, A., Williams, L., Ehn, M., Mikkilä, J., Canagaratna, M., Brune,

889   W., Onasch, T., and Jayne, J.: Relationship between aerosol oxidation level and hygroscopic

890   properties of laboratory generated secondary organic aerosol (SOA) particles, Geophys. Res. Lett.,

891   37, 2010.

892   May, A. A., Levin, E. J. T., Hennigan, C. J., Riipinen, I., Lee, T., Collett Jr., J. L., Jimenez, J.

893   L., Kreidenweis, S. M., and Robinson, A. L.: Gas-particle partitioning of primary organic aerosol

894   emissions: 3. Biomass burning, J. Geophys. Res. Atmos., 118, 11,327-311,338,

895   https://doi.org/10.1002/jgrd.50828, 2013.

896   Mei, F., Setyan, A., Zhang, Q., and Wang, J.: CCN activity of organic aerosols observed

897 downwind of urban emissions during CARES, Atmos. Chem. Phys., 13, 12155-12169, 2013.

898   Meng, J. W., Yeung, M. C., Li, Y. J., Lee, B. Y. L., and Chan, C. K.: Size-resolved cloud

899 condensation nuclei (CCN) activity and closure analysis at the HKUST Supersite in Hong Kong,

900 Atmos. Chem. Phys., 14, 10267-10282, 10.5194/acp-14-10267-2014, 2014.

901   Mochida, M., Kuwata, M., Miyakawa, T., Takegawa, N., Kawamura, K., and Kondo, Y.:

902 Relationship between hygroscopicity and cloud condensation nuclei activity for urban aerosols in

903 Tokyo, J. Geophys. Res., 111, D23204, 10.1029/2005jd006980, 2006.

904   Onasch, T. B., Trimborn, A., Fortner, E. C., Jayne, J. T., Kok, G. L., Williams, L. R., Davidovits,

905 P., and Worsnop, D. R.: Soot Particle Aerosol Mass Spectrometer: Development, Validation, and

906 Initial Application, Aerosol Sci. Tech., 46, 804-817, 10.1080/02786826.2012.663948, 2012.

907   Ovadnevaite, J., Zuend, A., Laaksonen, A., Sanchez, K. J., Roberts, G., Ceburnis, D., Decesari,

908 S., Rinaldi, M., Hodas, N., Facchini, M. C., Seinfeld, J. H., and O' Dowd, C.: Surface tension

909 prevails over solute effect in organic-influenced cloud droplet activation, Nature, 546, 637-641,

910 10.1038/nature22806, 2017.

911   Paatero, P., and Tapper, U.: Positive matrix factorization: A non-negative factor model with

912 optimal utilization of error estimates of data values, Environmetrics, 5, 111-126,

913 10.1002/env.3170050203, 1994.

914   Paatero, P.: Least squares formulation of robust non-negative factor analysis, Chemometr Intell

915 Lab, 37, 23-35, 10.1016/S0169-7439(96)00044-5, 1997.

916   Pajunoja, A., Lambe, A. T., Hakala, J., Rastak, N., Cummings, M. J., Brogan, J. F., Hao, L.,

917 Paramonov, M., Hong, J., and Prisle, N. L.: Adsorptive uptake of water by semisolid secondary

918 organic aerosols, Geophys. Res. Lett., 42, 3063-3068, 2015.

919   Park, S. H., Rogak, S. N., and Grieshop, A. P.: A Two-Dimensional Laminar Flow Model for

920 Thermodenuders Applied to Vapor Pressure Measurements, Aerosol Sci. Technol., 47, 283-293,

921 10.1080/02786826.2012.750711, 2013.

922   Petters, M., and Kreidenweis, S.: A single parameter representation of hygroscopic growth and

923 cloud condensation nucleus activity, Atmos. Chem. Phys., 7, 1961-1971, 2007.

924   Petters, M. D., Wex, H., Carrico, C. M., Hallbauer, E., Massling, A., McMeeking, G. R.,

925 Poulain, L., Wu, Z., Kreidenweis, S. M., and Stratmann, F.: Towards closing the gap between

926 hygroscopic growth and activation for secondary organic aerosol – Part 2: Theoretical approaches,

927 Atmos. Chem. Phys., 9, 3999-4009, 10.5194/acp-9-3999-2009, 2009.

928 Petters, M., and Kreidenweis, S.: A single parameter representation of hygroscopic growth and

929 cloud condensation nucleus activity–Part 3: Including surfactant partitioning, Atmos. Chem. Phys.,

930 13, 1081-1091, 2013.

931 Philippin, S., Wiedensohler, A., and Stratmann, F.: Measurements of non-volatile fractions of

932 pollution aerosols with an eight-tube volatility tandem differential mobility analyzer (VTDMA-8),

933 J. Aerosol Sci., 35, 185-203, http://dx.doi.org/10.1016/j.jaerosci.2003.07.004, 2004.

934 Qin, Y. M., Tan, H. B., Li, Y. J., Schurman, M. I., Li, F., Canonaco, F., Prévôt, A. S. H., and

935 Chan, C. K.: The role of traffic emissions in particulate organics and nitrate at a downwind site in

936 the periphery of Guangzhou, China, Atmos. Chem. Phys., 1-31, 2017.

937 Rastak, N., Pajunoja, A., Acosta Navarro, J. C., Ma, J., Song, M., Partridge, D. G., Kirkevåg,

938 A., Leong, Y., Hu, W. W., Taylor, N. F., Lambe, A., Cerully, K., Bougiatioti, A., Liu, P., Krejci, R.,

939 Petäjä, T., Percival, C., Davidovits, P., Worsnop, D. R., Ekman, A. M. L., Nenes, A., Martin, S.,

940 Jimenez, J. L., Collins, D. R., Topping, D. O., Bertram, A. K., Zuend, A., Virtanen, A., and Riipinen,

941 I.: Microphysical explanation of the RH-dependent water affinity of biogenic organic aerosol and

942 its importance for climate, Geophys. Res. Lett., 44, 5167-5177, 10.1002/2017GL073056, 2017.

943 Renbaum-Wolff, L., Song, M., Marcolli, C., Zhang, Y., Liu, P. F., Grayson, J. W., Geiger, F. M.,

944 Martin, S. T., and Bertram, A. K.: Observations and implications of liquid–liquid phase separation at high

945 relative humidities in secondary organic material produced by α-pinene ozonolysis without inorganic

946 salts, Atmos. Chem. Phys., 16, 7969-7979, 10.5194/acp-16-7969-2016, 2016.

947 Riipinen, I., Pierce, J. R., Donahue, N. M., and Pandis, S. N.: Equilibration time scales of

948 organic aerosol inside thermodenuders: Evaporation kinetics versus thermodynamics, Atmos.

949 Environ., 44, 597-607, https://doi.org/10.1016/j.atmosenv.2009.11.022, 2010.

950 Rose, D., Gunthe, S., Mikhailov, E., Frank, G., Dusek, U., Andreae, M. O., and Pöschl, U.:

951 Calibration and measurement uncertainties of a continuous-flow cloud condensation nuclei counter

952 (DMT-CCNC): CCN activation of ammonium sulfate and sodium chloride aerosol particles in theory

953 and experiment, Atmospheric Chemistry and Physics, 8, 1153-1179, 2008.

954   Rose, D., Nowak, A., Achtert, P., Wiedensohler, A., Hu, M., Shao, M., Zhang, Y., Andreae, M.

955   O., and Pöschl, U.: Cloud condensation nuclei in polluted air and biomass burning smoke near the

956   mega-city Guangzhou, China – Part 1: Size-resolved measurements and implications for the

957   modeling of aerosol particle hygroscopicity and CCN activity, Atmos. Chem. Phys., 10, 3365-3383,

958   10.5194/acp-10-3365-2010, 2010.

959   Ruehl, C. R. and Wilson, K. R.: Surface organic monolayers control the hygroscopic growth of

960   submicrometer particles at high relative humidity, The Journal of Physical Chemistry A, 118, 3952-3966,

961   2014.

962   Saha, P. K., Khlystov, A., Grieshop, A. P.: Determining aerosol volatility parameters using a

963   "Dual Thermodenuder" system: application to laboratory-generated organic aerosols, Aerosol Sci.

964   Tech., 49, 620-632, 2015.

965   Saha, P. K., Khlystov, A., Yahya, K., Zhang, Y., Xu, L., Ng, N. L., Grieshop, A. P.: Quantifying

966   the volatility of organic aerosol in the southeastern US, Atmos. Chem. Phys., 17, 501-520, 2017.

967   Saleh, R., Walker, J., and Khlystov, A.: Determination of saturation pressure and enthalpy of

968   vaporization of semi-volatile aerosols: The integrated volume method, J. Aerosol Sci.e, 39, 876-887,

969   https://doi.org/10.1016/j.jaerosci.2008.06.004, 2008.

970   Schill, G. P. and Tolbert, M. A.: Heterogeneous ice nucleation on phase-separated organic-sulfate

971   particles: effect of liquid vs. glassy coatings, Atmos. Chem. Phys., 13, 4681-4695, 10.5194/acp-13-4681-

972   2013, 2013.

973   Schill, G. P. and Tolbert, M. A.: Heterogeneous ice nucleation on phase-separated organic-sulfate

974   particles: effect of liquid vs. glassy coatings, Atmos. Chem. Phys., 13, 4681-4695, 10.5194/acp-13-4681-

975   2013, 2013.

976   Seinfeld, J. H., and Pandis, S. N.: Atmospheric chemistry and physics: from air pollution to

977   climate change, John Wiley & Sons, 2016.

978   Shrivastava, M., Cappa, C. D., Fan, J., Goldstein, A. H., Guenther, A. B., Jimenez, J. L., Kuang,

979   C., Laskin, A., Martin, S. T., Ng, N. L., Petaja, T., Pierce, J. R., Rasch, P. J., Roldin, P., Seinfeld, J.

980   H., Shilling, J., Smith, J. N., Thornton, J. A., Volkamer, R., Wang, J., Worsnop, D. R., Zaveri, R. A.,

981   Zelenyuk, A., and Zhang, Q.: Recent advances in understanding secondary organic aerosol:

982   Implications   for   global   climate   forcing,   Rev.   Geophys.,   55,   509-559,

983   https://doi.org/10.1002/2016RG000540, 2017.

984   Song, M., Marcolli, C., Krieger, U. K., Zuend, A., and Peter, T.: Liquid-liquid phase separation and

985   morphology of internally mixed dicarboxylic acids/ammonium sulfate/water particles, Atmos. Chem.

986   Phys., 12, 2691-2712, 10.5194/acp-12-2691-2012, 2012a.

987   Song, M., Marcolli, C., Krieger, U. K., Zuend, A., and Peter, T.: Liquid-liquid phase separation in

988   aerosol particles: Dependence on O:C, organic functionalities, and compositional complexity, Geophys.

989   Res. Lett., 39, https://doi.org/10.1029/2012GL052807, 2012b.

990   Stokes, R., and Robinson, R.: Interactions in aqueous nonelectrolyte solutions. I. Solute-

991   solvent equilibria, J. Phys. Chem., 70, 2126-2131, 1966.

992   Stolzenburg, M. R., and McMurry, P. H.: Equations Governing Single and Tandem DMA

993   Configurations and a New Lognormal Approximation to the Transfer Function, Aerosol Sci. Tech.,

994   42, 421-432, 10.1080/02786820802157823, 2008.

995   Sun, Y. L., Zhang, Q., Schwab, J. J., Yang, T., Ng, N. L., and Demerjian, K. L.: Factor analysis

996   of combined organic and inorganic aerosol mass spectra from high resolution aerosol mass

997   spectrometer measurements, Atmos. Chem. Phys., 12, 8537-8551, 10.5194/acp-12-8537-2012,

998   2012.

999   Tan, H., Xu, H., Wan, Q., Li, F., Deng, X., Chan, P. W., Xia, D., and Yin, Y.: Design and

1000   Application of an Unattended Multifunctional H-TDMA System, J. Atmos. Oceanic Tech., 30, 1136-

1001   1148, 10.1175/JTECH-D-12-00129.1, 2013a.

1002   Tan, H., Yin, Y., Gu, X., Li, F., Chan, P. W., Xu, H., Deng, X., and Wan, Q.: An observational

1003   study of the hygroscopic properties of aerosols over the Pearl River Delta region, Atmos. Environ.,

1004   77, 817-826, http://dx.doi.org/10.1016/j.atmosenv.2013.05.049, 2013b.

1005   Thalman, R., Sá, S. S. d., Palm, B. B., Barbosa, H. M., Pöhlker, M. L., Alexander, M. L., Brito,

1006   J., Carbone, S., Castillo, P., Day, D. A.: CCN activity and organic hygroscopicity of aerosols

1007   downwind of an urban region in central Amazonia: seasonal and diel variations and impact of

1008   anthropogenic emissions, Atmos. Chem. Phys., 17, 11779-11801, 2017.

1009   Ulbrich, I. M., Canagaratna, M. R., Zhang, Q., Worsnop, D. R., and Jimenez, J. L.:

1010   Interpretation of organic components from Positive Matrix Factorization of aerosol mass

1011   spectrometric data, Atmos. Chem. Phys., 9, 2891-2918, 10.5194/acp-9-2891-2009, 2009.

1012   Volkamer, R., Jimenez, J. L., Martini, F. S., Dzepina, K., Qi, Z., Salcedo, D., Molina, L. T.,

1013   Worsnop, D. R., and Molina, M. J.: Secondary organic aerosol formation from anthropogenic air

1014   pollution: Rapid and higher than expected, Geophys. Res. Lett., 33, 254-269, 2006.

1015   Wang, D. S., and Hildebrandt Ruiz, L.: Chlorine-initiated oxidation of n-alkanes under high-

1016   NOx conditions: insights into secondary organic aerosol composition and volatility using a

1017   FIGAERO–CIMS, Atmos. Chem. Phys., 18, 15535-15553, 10.5194/acp-18-15535-2018, 2018.

1018   Wang, J., Lee, Y. N., Daum, P. H., Jayne, J., and Alexander, M. L.: Effects of aerosol organics

1019   on cloud condensation nucleus (CCN) concentration and first indirect aerosol effect, Atmos. Chem.

1020   Phys., 8, 6325-6339, 10.5194/acp-8-6325-2008, 2008.

1021   Wang, J., Cubison, M., Aiken, A., Jimenez, J., and Collins, D.: The importance of aerosol

1022   mixing state and size-resolved composition on CCN concentration and the variation of the

1023   importance with atmospheric aging of aerosols, Atmos. Chem. Phys., 10, 7267-7283, 2010.

1024   Wex, H., Petters, M. D., Carrico, C. M., Hallbauer, E., Massling, A., McMeeking, G. R., Poulain,

1025   L., Wu, Z., Kreidenweis, S. M., and Stratmann, F.: Towards closing the gap between hygroscopic growth

1026   and activation for secondary organic aerosol: Part 1 – Evidence from measurements, Atmos. Chem. Phys.,

1027   9, 3987-3997, 10.5194/acp-9-3987-2009, 2009.

1028   Wu, Z. J., Poulain, L., Henning, S., Dieckmann, K., Birmili, W., Merkel, M., van Pinxteren,

1029   D., Spindler, G., Müller, K., Stratmann, F., Herrmann, H., and Wiedensohler, A.: Relating particle

1030   hygroscopicity and CCN activity to chemical composition during the HCCT-2010 field campaign,

1031   Atmos. Chem. Phys., 13, 7983-7996, 10.5194/acp-13-7983-2013, 2013.

1032   Xu, W., Chen, C., Qiu, Y., Xie, C., Chen, Y., Ma, N., Xu, W., Fu, P., Wang, Z., Pan, X., Zhu, J.,

1033   Ng, N. L., and Sun, Y.: Size-resolved characterization of organic aerosol in the North China Plain:

1034   new insights from high resolution spectral analysis, Environ. Sci. Atmos., 1, 346-358,

1035   10.1039/D1EA00025J, 2021.

1036   Xu, W., Xie, C., Karnezi, E., Zhang, Q., Wang, J., Pandis, S. N., Ge, X., Zhang, J., An, J., Wang,

1037   Q., Zhao, J., Du, W., Qiu, Y., Zhou, W., He, Y., Li, Y., Li, J., Fu, P., Wang, Z., Worsnop, D. R., and

1038   Sun, Y.: Summertime aerosol volatility measurements in Beijing, China, Atmos. Chem. Phys., 19,

1039   10205-10216, 10.5194/acp-19-10205-2019, 2019.

1040   Yuan, L., Zhang, X., Feng, M., Liu, X., Che, Y., Xu, H., Schaefer, K., Wang, S., and Zhou, Y.:

Size-resolved hygroscopic behaviour and mixing state of submicron aerosols in a megacity of the Sichuan Basin during pollution and fireworks episodes, Atmos. Environ., 226, 117393, https://doi.org/10.1016/j.atmosenv.2020.117393, 2020.

Zdanovskii, A.: NOVYI METOD RASCHETA RASTVORIMOSTEI ELEKTROLITOV V MNOGOKOMPONENTNYKH SISTEMAKH. 1, Zhurnal Fizicheskoi Khimii, 22, 1478-1485, 1948.

Zhang, Q., Canagaratna, M. R., Jayne, J. T., Worsnop, D. R., and Jimenez, J. L.: Time-and size-resolved chemical composition of submicron particles in Pittsburgh: Implications for aerosol sources and processes, J. Geophys. Res. Atmos., 1984–2012, 110, 2005a.

Zhang, Q., Worsnop, D. R., Canagaratna, M. R., and Jimenez, J. L.: Hydrocarbon-like and oxygenated organic aerosols in Pittsburgh: insights into sources and processes of organic aerosols, Atmos. Chem. Phys., 5, 3289-3311, 10.5194/acp-5-3289-2005, 2005b.

Zhang, Y., Tao, J., Ma, N., Kuang, Y., Wang, Z., Cheng, P., Xu, W., Yang, W., Zhang, S., Xiong, C., Dong, W., Xie, L., Sun, Y., Fu, P., Zhou, G., Cheng, Y., and Su, H.: Predicting cloud condensation nuclei number concentration based on conventional measurements of aerosol properties in the North China Plain, Sci. Tot. Environ., 719, 137473, https://doi.org/10.1016/j.scitotenv.2020.137473, 2020.

Zhao, D. F., Buchholz, A., Kortner, B., Schlag, P., Rubach, F., Kiendler-Scharr, A., Tillmann, R., Wahner, A., Flores, J. M., Rudich, Y., Watne, Å. K., Hallquist, M., Wildt, J., and Mentel, T. F.: Size-dependent hygroscopicity parameter (κ) and chemical composition of secondary organic cloud condensation nuclei, Geophys. Res. Lett., 42, 10,920-910,928, https://doi.org/10.1002/2015GL066497, 2015.

Zhao, D. F., Buchholz, A., Kortner, B., Schlag, P., Rubach, F., Fuchs, H., Kiendler-Scharr, A., Tillmann, R., Wahner, A., Watne, Å. K., Hallquist, M., Flores, J. M., Rudich, Y., Kristensen, K., Hansen, A. M. K., Glasius, M., Kourtchev, I., Kalberer, M., and Mentel, T. F.: Cloud condensation nuclei activity, droplet growth kinetics, and hygroscopicity of biogenic and anthropogenic secondary organic aerosol (SOA), Atmos. Chem. Phys., 16, 1105-1121, 10.5194/acp-16-1105-2016, 2016.

1069 Table 1. The density and the κ value of the related species used in this study.

Species	Density (kg m^{-3})	κ
NH$_4$NO$_3$	1720[a]	0.58[b]
NH$_4$HSO$_4$	1780[a]	0.56[b]
H$_2$SO$_4$	1830[a]	0.90[b]
(NH$_4$)$_2$SO$_4$	1769[a]	0.48[b]
Organics	1400[a]	0.10[b]
BC	1770[c]	0[d]

1070   [a] From Gysel et al. (2007); [b] From (Cai et al., 2018); [c] From Deng et al. (2019); [d] Assumed to be 0.

1071

1072 Table 2. Thermophysical properties of each component used in the multi-component evaporation

1073 dynamics model.

Parameters	ELVOA	LVOA	SVOA	Ammonium Nitrate	Ammonium Sulfate	Black Carbon
$C_i^*(T_{ref})$ (µg m^{-3}) [a]	10^{-5}	10^{-2}	10	76	2×10^{-3}	10^{-30}
D_i (m^2 s^{-1}) [b]	5×10^{-6}	5×10^{-6}	5×10^{-6}	5×10^{-6}	5×10^{-6}	5×10^{-6}
$\sigma_{s/a}$ (N m^{-1}) [c]	0.05	0.05	0.05	0.05	0.05	0.05
M_i (kg mol^{-1})	0.2	0.2	0.2	0.08	0.132	0.28
ρ_i (kg m^{-3})	1400	1400	1400	1720	1769	1770
$\Delta H_{vap,i}$ (kJ mol^{-1}) [d]	80	80	80	152	94	100
α [e]	0.09	0.09	0.09	0.09	0.09	0.09

1074 [a] From Hong et al. (2017); [b] From Riipinen et al. (2010); [c] From Riipinen et al. (2010); [d] The ΔH_{vap}

1075 values of organics are obtained from the sensitivity test shown in Fig. S4 and the values of inorganic

1076 species are from Hong et al. (2017); [e] Obtained from the sensitivity test shown in Fig. S4.

1077

1078   Table 3. The average and standard deviation values (mean±std) of N_{CCN}, AR, D_{50}, and κ_{CCN} at 0.1%,

1079   0.2%, 0.4%, 0.7%, 0.9% and 1.0% SS during the campaign.

SS	0.1%	0.2%	0.4%	0.7%	0.9%	1.0%
N_{CCN} (# cm^{-3})	2507±1187	4322±1981	5843±2461	6834±2921	7497±3210	7862±3352
AR	0.20±0.09	0.34±0.13	0.45±0.16	0.52±0.17	0.57±0.17	0.60±0.17
D_{50} (nm)	145.55±11.26	92.83±8.80	66.79±6.33	52.56±5.46	45.38±4.82	42.26±4.45
κ_{CCN}	0.48±0.13	0.47±0.15	0.31±0.10	0.22±0.09	0.20±0.08	0.20±0.08

1080

1081   FIGURE CAPTIONS

1082   Figure 1. The temporal profile of the measured variables during the campaign. (a) particle number

1083   size distribution; (b) PM_1 chemical composition measured by the SP-AMS along with mass

1084   concentration of $PM_{2.5}$; (c) mass fraction of each species; (d) wind speed and direction. The color

1085   code in (d) represents the wind direction.

1086   Figure 2. The temporal profile of GF-PDF at the measured diameters (30, 50, 80, 100, 150 and 200

1087   nm). The color code denotes the probability density and the red solid line represents the mean GF

1088   (GF_{mean}).

1089   Figure 3. The average mass fraction distribution of SVOA, LVOA and ELVOA at the measured

1090   diameters (30, 50, 80, 100, 150 and 200 nm), and average size-resolved hygroscopicity of organic

1091   aerosol (κ_{OA}) with the upper and lower error bars (in red).

1092   Figure 4. The campaign average diurnal variation of mass fraction of organics and f44 in bulk

1093 PM_1 (a), the κ values at 200 nm obtained by HTDMA (κ_{HTDMA}) and AMS (κ_{AMS}) measurements

1094   (b), the PNSD (c) and mass distribution of organics (d). The shaded area represents standard

1095   deviation.

1096   Figure 5. The diurnal variation (displayed in boxplot) mass concentration of the deconvolved OA

1097   factors from PMF analysis of AMS data, including more oxygenated OA (MOOA), less

1098   oxygenated OA (LOOA), aged biomass burning OA (aBBOA), hydrocarbon-like OA (HOA),

1099   biomass burning OA (BBOA), and nighttime OA (night-OA).

1100   Figure 6. The average (solid line) and standard deviation (shaded area) diurnal variation of κ_{OA} at

1101   different particle diameters.

1102   Figure 7. The size-resolved volatility distribution during daytime (8:00-16:00 LT) and nighttime

1103   (20:00 to 4:00 LT) based on the median time of each cycle owing to the limited time resolution.

1104   Figure 8. The average diurnal variation of $\delta_{N_{CCN}}$ at 0.1%, 0.2%, 0.4% and 0.7% SS based on fixed

1105 κ_{OA} (a), SR κ_{OA} (b) and SR diurnal κ_{OA} (c).

1106
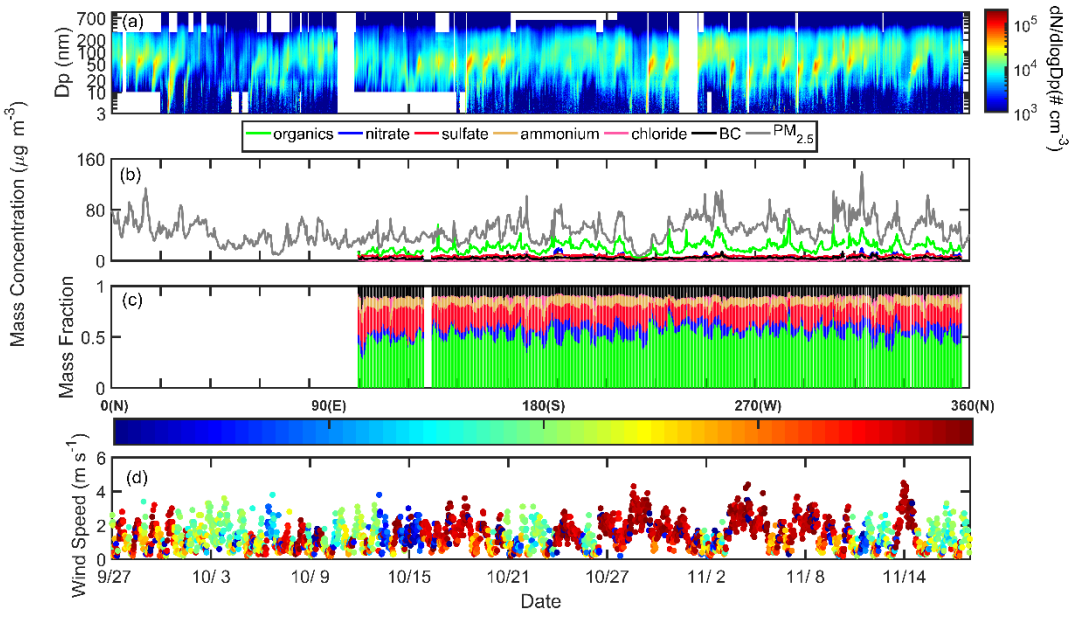
1107

1108

1109

1110   Fig. 1.

1111

1112

1113   Fig. 2.

1114
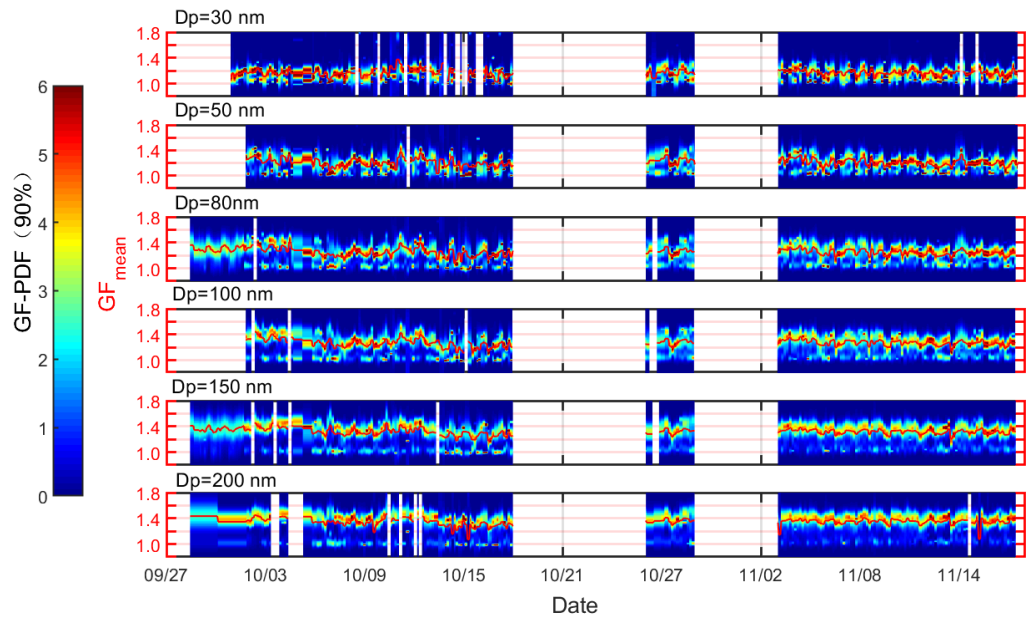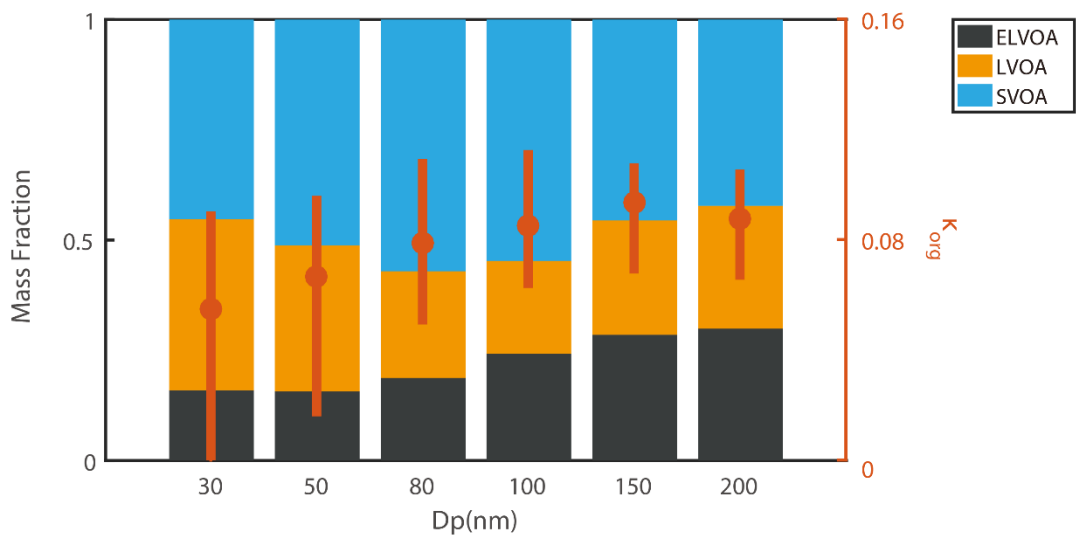
1115

1116

1117   Fig. 3.

1118
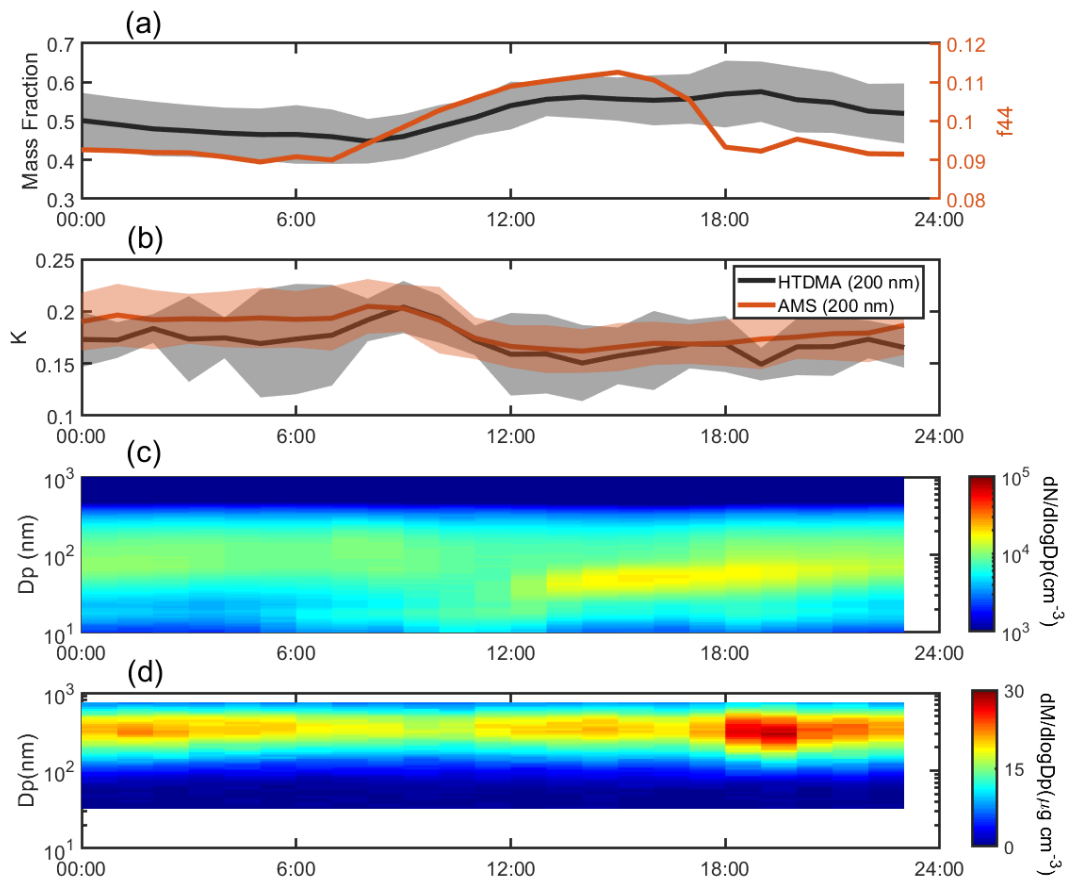
1119

1120

1121   Fig. 4.

1122
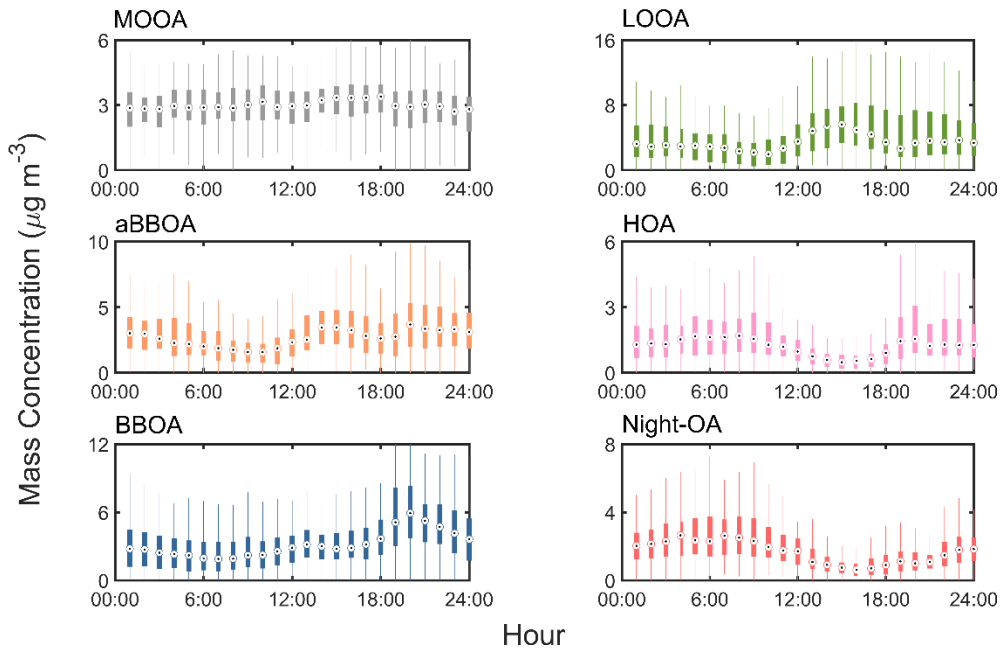
1123

1124

1125   Fig. 5.
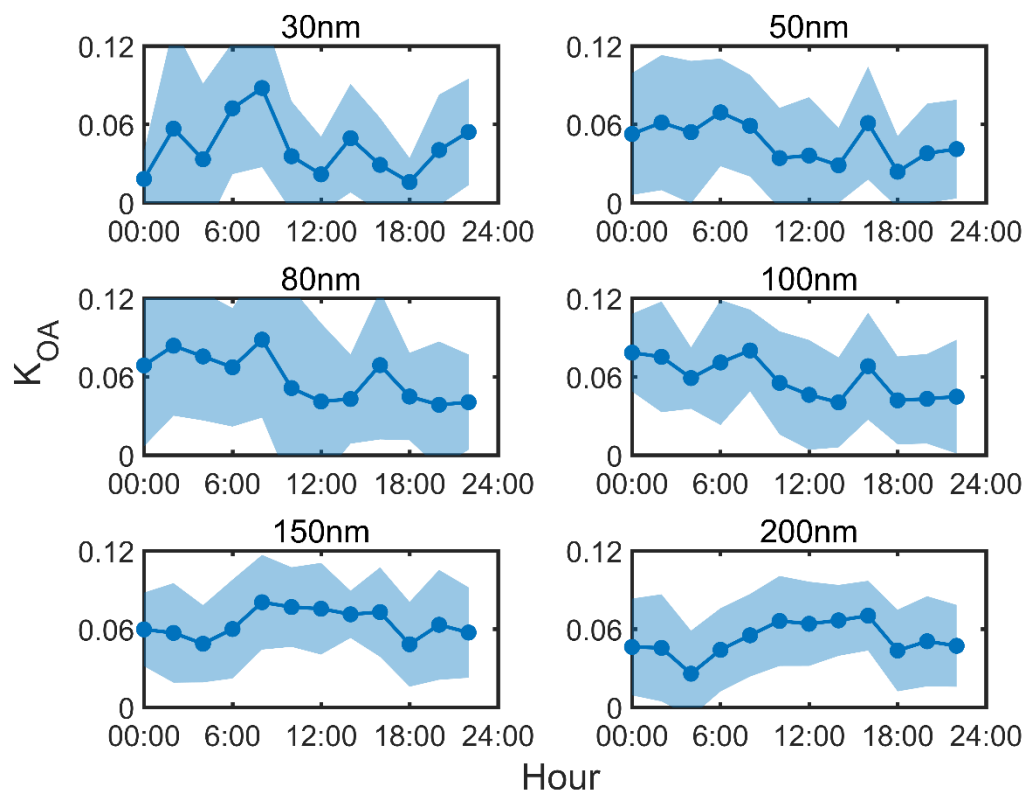
1126

1127

1128   Fig. 6.
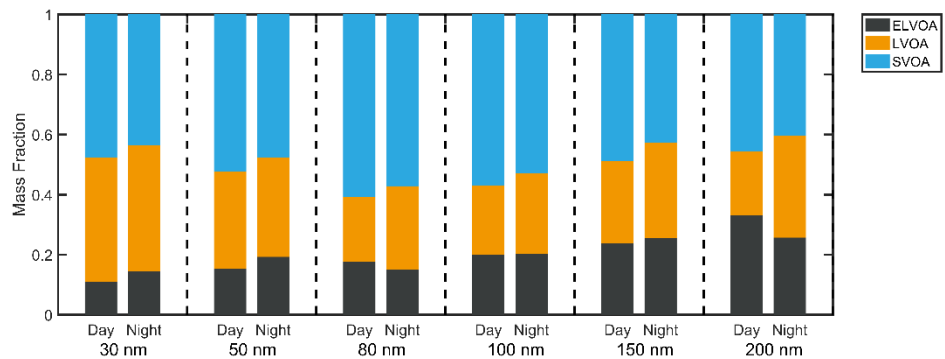
1129

1130

1131   Fig. 7.

1132

1133

1134

1135

1136   Fig. 8.